Patient-Specific Finite Element Modeling of Bones from X-ray Images based on Computer-Tomography Databases

Von der Fakultät für Bauingenieurwesen und Geodäsie

der Gottfried Wilhelm Leibniz Universität Hannover

zur Erlangung des akademischen Grades

Doktor - Ingenieur

genehmigte Dissertation

von

M. Sc. Ehsan Jamshidi

2016

Hauptreferent:

Prof. Dr.-Ing. habil. U. Nackenhorst

Korreferent:

Prof. Dr.-Ing. habil. V. Berkhahn

Tag der Promotion:

31.08.2016

Preface

Novelties in this work are introducing three approaches. The first one is the step 11 of the framework for reconstruction of 3D models from 2D images, Fig. 1.1. The novelty is using a criterion based on a best-matching model, §2.2.6, instead of a common modification approach found in the literature. The second one and the third one are introducing new error tests, §3.2.2 and §3.2.4, and a method to calibrate CT scanners instead of CT scans, §4.3.2.

To implement the introduced approach for building 3D CAD models from 2D images, one may follow the steps in the Fig. 1.1 explained in the appendix A. Parameters that are initialized during following the instructions, have been described in §§2.2.2-2.2.7.

To analyze accuracy of the built model, chapter three should be read. If tests 3.2.1 and 3.2.3 are performed, one can compare the results with former works. Tests 3.2.2 and 3.2.4 are new and an interpretation of them can be found in the discussion, §3.3.

To assign the patient-specific material properties to the built model, in case one has access to a relevant calibration phantom image, he may follow the instructions in Fig. 4.1. Otherwise, an approach is suggested in §4.3.2. The method is very simple yet it enables to obtain the patient-specific density distributions from CT datasets which contain no calibration images, a task that previously might be impossible.

Acknowledgments

During the last three years, required elements for my research were provided to me thanks to the MARIO scholarship from the government of the Lower Saxony state, the IBNM institute, and the MUSIC graduate school.

I would like to sincerely thank Prof. Dr.-Ing. habil. Udo Nackenhorst and Prof. Dr. med Gabriala von Lewinski as they accepted my mentorship, gave me their priceless recommendations at the most humble manner and helped me in all issues as fast as it was possible. I also have a special thanks to Prof. Lewinski that granted me a wide CT dataset of patients and a chance to visit a hip joint replacement surgery in the operation room. In addition, I am honorable that Prof. Dr.-Ing. habil. Volker Berkhahn accepted to be the referee of my thesis and I am thankful to Prof. Dr. rer. nat. Insa Neuweiler who served as the president of the dissertation committee.

I would like to thank my colleagues and friends at the MARIO, the IBNM, and the IKM who we shared together good memories during seminars, sport events, ceremonies, and birthday parties.

Finally, I thank my Adored Parents who always ignored their favorites to provide the best possible situation for my education without any expectations.
Thank you,

Hannover, 30 June 2016   Ehsan Jamshidi

Abstract

In this work, three new approaches are presented from which the first two are: a method for creating 3D CAD bone models using 2D images and investigating its accuracy via applying new tests. Previous approaches were based on building a mean model from a dataset of patients' bone models and then modifying it in order to properly resemble provided 2D images of a new patient. Although this strategy is popular among researchers, it is still a challenge to modify the mean model in the views where the new patient possesses no 2D image. That difficulty comes from the fact that the bone shape is a patient-specific characteristic influenced by several parameters while a mathematical relationship is not available as a connection between these parameters and the bone outline.

As a solution to overcome this trouble, statistical mean models are not employed in the present method, rather the method is based on the similarity between geometry of bones. Its assumption is when specific parts of two bones are similar in one view, they have experienced the same physiological history and, consequently, they are similar in other views as well. After explaining the method, its accuracy is analyzed with common tests and two new ones: one test to determine offset error of the method and another test to study quantitative relationships between reconstruction errors and stress values on the simulated bone models.

For assigning mechanical properties to the reconstructed 3D models in a patient-specific manner, in the selected approach in this work, a calibration

phantom during the CT scanning of the patient is scanned as well. Afterwards, a relationship between image intensities and bone mechanical properties is established using image processing techniques and experimental results. Through this strategy, each voxel and, consequently, the bone model is attributed the properties.

Although the method is straightforward, it is faced with an obstacle which is lack of calibration images in CT datasets. To solve this problem, a method is proposed to calibrate previous scans of CT machines. The solution originates from this view that instead of calibrating CT scans at each screening, the CT machine is calibrated once and the obtained relationships are used thereafter.

Keywords: Patient-specific 3D finite element model, Statistical shape models, 3D reconstruction, Calibration phantom

Zusammenfassung

In dieser Arbeit werden zwei Beiträge vorgestellt. Die Beiträge sind neue Ansätze zur Erstellung von 3D-CAD-Knochen-Modellen unter Verwendung von 2D-Bildern, sowie neue Tests zur Untersuchung der Genauigkeits des Verfahrens. Bisherige Ansätze basieren auf der Erstellung eines statistischen Modells (SSM) anhand der Datensätze von Patienten Knochenmodellen und der anschließenden Modifizierung, um dieses den zur Verfügung gestellt 2D-Bilder eines neuen Patienten anzugleichen.

Obwohl diese Strategie weit verbreitet ist, ist es immer noch eine Herausforderung das SSM in den Ansichten anzupassen, von denen keine 2D-Bilder des neuen Patienten existieren. Die Schwierigkeit beruht auf der Tatsache, dass die Knochenform durch die patienten-spezifischen physiologische Geschichte beeinflußten wird, während keine mathematische Beziehung als Verbindung zwischen diesen Parametern und dem Knochen zur Verfügung steht.

Der Ansatz zur Lösung dieses Problems basiert darauf, dass die SSM nicht auf der dargestellten Methode, sondern das Verfahren auf der Ähnlichkeit der Geometrie von Knochen beruht. Es wird die folgende Annahme getroffen: wenn spezifischen Teile von zwei Knochen in einer Ansicht ähnlich sind, dann haben sie die gleiche physiologische Geschichte und sind sich folglich auch in anderen Bild-Ansichten ähnlich. Nach Erläuterung des Verfahrens wird seine Genauigkeit mit allgemeinen üblichen Tests und mit zwei neuen Tests analysiert: einem Test zur Bestimmung des Offsetfehlers und einem weiteren Test

um die quantitative Beziehungen zwischen den Rekonstruktionsfehler und den Spannungswerten der simulierten Knochen-Modelle zu studieren.

Eine Strategie um die Zuordnung mechanischer Eigenschaften auf die rekonstruierten 3D Modelle zu finden ist das Scannen eines Kalibrierphantoms während des CT-Scans eines Patienten. Danach wird eine Beziehung zwischen Bildintensität und mechanischen Eigenschaften der Knochen hergestellt unter Verwendung von Bildverarbeitungstechniken und experimentellen Ergebnissen. Durch diesen Ansatz wird jedes Voxel, und folglich auch das Knochenmodell den Eigenschaften zugeordnet.

Obwohl die Strategie relativ simpel ist, stellt die fehlenden Kalibrierung von Bildern aus CT-Datensätzen ein Hindernis dar. Um dieses Problem zu lösen, wird ein Verfahren vorgeschlagen, welches es ermöglicht vorherige Scans von CT-Maschinen zu kalibrieren. Der Ansatz zur Lösung ist, anstelle der Kalibrierung des CT-Scans bei jedem Screening wird das CT-Gerät einmal kalibriert und die erhaltenen Beziehungen daraufhin angewendet.

Stichwort: Patient-spezifischen 3D-Finite-Element Modell, Statistische Modells, 3D-Rekonstruktion, Kalibrierphantom

Contents

Chapter 1

Introduction

3D models of skeletal structures are required in numerous clinical treatments and it is acquired routinely by employing CT scans of patients. The procedure has been utilized in various applications, namely the implant design and numerical studies on alternative therapies (SAHA & ROYCHOWDHURY, 2009; LUTZ ET AL., 2011; BAH ET AL., 2015), the mechanical simulation of bone remodeling (LUTZ & NACKENHORST, 2012; TOMASZEWSKI ET AL., 2012; XU ET AL., 2016) and the mechanical analysis of skeletal muscles (JOHANSSON ET AL., 2000; MARTINS ET AL., 2006; TANG ET AL., 2009). However, to decrease the financial costs and the intensity of radiation to which patients are exposed, there are efforts to build the 3D models from 2D images while limiting them to as few as possible (PETKOVIĆ ET AL., 2014; VÄÄNÄNEN ET AL., 2015; KARADE & RAVI, 2015).

The general framework used by previous works to build a 3D model of a pa-

tient's bone from his x-ray images with the help of a CT dataset is displayed in Fig. 1.1. For convenience in the description, this figure is referred to as framework and its steps are cited by No. X. As the framework used images of former patients, they are required to be given and it is done by providing their CT scans, No. 1. Afterwards to build 3D models of the patients, No. 7, a series of actions are performed, namely for each CT set of a patient, its slices are segmented, No. 2, and a point distribution model (PDM) is obtained, No. 3. By statistical approaches, a statistical shape model (SSM) from the bones in the database is built at this step.

Thereafter in No. 4, a surface model is reconstructed on the PDMs and smoothened, No. 6. Models at No. 7 and No. 15 are called gold models as they are obtained from CT scans. By projecting each of the models, 2D views of the models are acquired, No. 9. They are then scaled, registered, and compared with the given 2D images of a new patient, No. 10. Afterwards, a modification process in the statistical approach or a selection process in the present work, is executed on them, No. 11. In No. 10, patient's DXA image can similarly be applied. The acquired PDM, No. 12, is undergone the same processes as before and results in the new patient's 3D bone model, No. 13. After achieving the 3D models, No. 7, No. 13, and No. 15, volumetric meshing and the Finite Element Analysis (FEA) can be executed on the models.

Among the published papers, there is one work that did not employ directly a mean shape from the dataset (THEVENOT ET AL., 2013). Instead, they measured

nine internal parameters for all bones in the dataset followed by establishing relationships between these parameters of each bone with radii[1] of landmarks on the surface. In the next step, the same nine parameters on the patient's x-ray image were measured and using the previously established relationships the radii of all points of the required 3D model were calculated. As radius of each point on the surface is needed to be calculated, applying the method for reconstruction of the whole femur is a laborious task and in practice, limits the method for reconstruction of small areas. Similar to SSM approaches, averaging of all models in the dataset to build the new model is present in this method as well.

The final 3D bone model created by following the framework's steps is not the same as the real bone model because of errors accumulated in each step. To investigate these error values, accuracy tests performed in the former works are classified in two types. In the first, accuracy of segmentation was considered and it was measured how much would be the difference between various segmented images (ROBERTS ET AL., 2006; ZHENG ET AL., 2009; GOOAYEN ET AL., 2011; ROBERTS ET AL., 2012; SARKALKAN ET AL., 2014a), i.e., if they performed a manual segmentation it was studied how much the reproducibility of the results would be when different users segment the CT sets.

If a semi-automatic segmentation is performed, the difference between a manual segmentation and the semi-automatic segmentation was studied. In the second type of the tests, it was examined how much would be the difference between

---

[1]By considering the neck and the shaft as cylinders, a kind of radius can be defined for the bone surface points.

two models built by the proposed method from 2D images and built from CT scans, comparison between No.13 and No. 15, called validation test.

Heart of all the statistical approaches is that a mean model is modified in a way that its projections resemble well the x-ray image of the new patient. Although this approach is common among researchers, no work took into account the diversity of ethnics, genders and ages of patients in the dataset during the mean model reconstruction, while MAHFOUZ ET AL. (2012) reported different mean shapes in their studied populations, African-American[2] and East Asian populations as compared to the Caucasian population.

Based on this research result, an improved procedure to use SSMs would be: first, the dataset is classified into different ages, genders, and ethnicities. Thereafter, the corresponding mean model, No. 3, is reconstructed for each group. New patient's x-ray image is then placed in the most relative group and compared with projections of the mean model of that group, No. 9. Nonetheless, former works have used one mean model for the whole dataset.

The reason that they did not report large reconstruction errors could be that their used datasets and test groups consisted of patients' images in a not large range of ages, in the range of 50 to 85 year-old. Also as they did not report patients' ethnic background, it is concluded the used database did not include diversity in this aspect. Therefore, by applying these methods that are based on one mean model on a dataset containing different ethnicities, the reconstruction error might
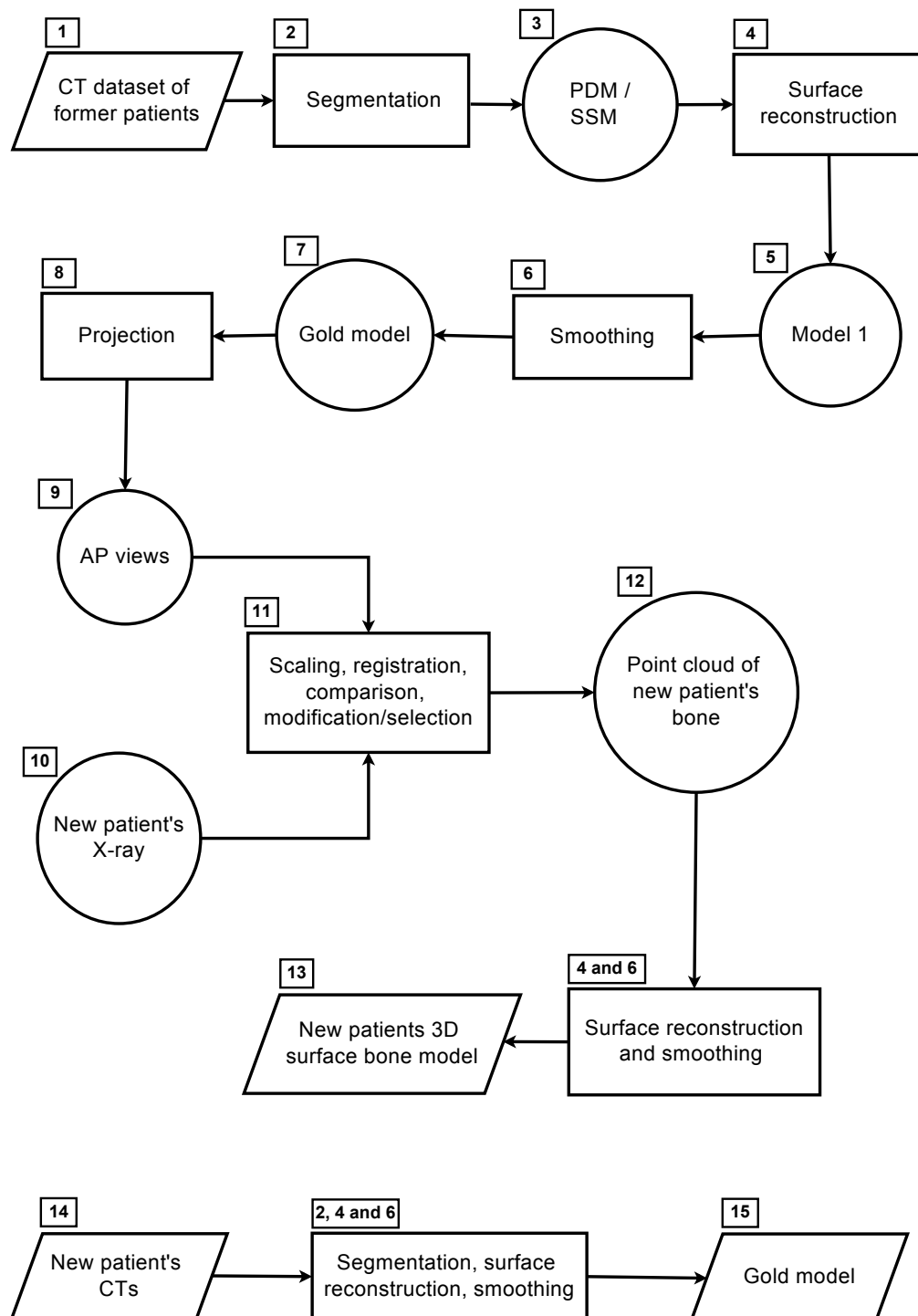
---

[2]Black Americans

Figure 1.1: Schematic representation of the steps in the methods that reconstruct a 3D model from x-ray images of a patient's bone based on a CT dataset.

become larger. Another reason that former works used one mean model for the whole of dataset is the high computational cost of building distinct models for each group. To avoid using this not cost effective approach, a possible solution would be creating the SSM using a training dataset mixed of patients with different ethnic backgrounds. However, there are two points about using this approach. First, how the training database should be created to be an optimal choice is still an open question. Second, how accurately a mean shape built on this database can represent variations of the individuals in different ethnic groups has not been addressed yet (SARKALKAN ET AL., 2014b).

The major challenge to employ SSMs arises during the modification procedure, No. 11. When a mean model is modified in one view to become similar to the patient's x-ray image, other views of the mean model are still affected by all bones in the dataset, without considering their level of similarity to the patient's bone. In fact, since the bone shape is influenced by complicated parameters, implementing a reasonable modification on the other views might be impossible as there is no mathematical relationship available as a connection between these parameters and the bone outline.

As a solution to overcome this issue, statistical mean models are not employed in the present work. The approach is based on the similarity between different bone geometries, §2.2.6. When specific parts of two bones match in one view, it is concluded that they have experienced similar physiological history and, consequently, they are taken to be similar in other views as well. This conclusion

comes from the fact that bone's shape is adapted to the acting force on it.

In chapter 3, new tests to analyze accuracy of the framework are presented. In the first test, arisen error in each of the steps is investigated, §3.2.1. The results show that the smoothing's error could be larger than the segmentation's. It might be argued that if another smoothing method is applied, the error might become smaller. This can be true but what the author suggests is that researchers in the field of 3D reconstruction should evaluate reproducibility of all the steps. Currently this investigation is performed only for the segmentation.

In the second suggested test, a method is introduced that measures the offset error of the proposed methods, §3.2.2. In the third proposed test, the changes in amount of stress values due to reconstruction errors are measured[3], §3.2.4. The procedure for this test is that two reconstructed bones of a patient, one built from CTs and one from 2D images, are undergone a same simulation, i.e., similar loading conditions and geometrical boundary conditions are applied to the both models. Then differences between stress values at the same areas are measured, e.g., where the maximum stress has happened in the reconstructed model from CTs. Using Hausdorff criterion, distances between these areas are also measured. Combination of these two measurements gives a new information that how much reconstruction error causes how much changes in the stresses.

In the last chapter, a method is presented that enables to calibrate CT scans of CT

---

[3]The validation test, §3.2.3, has been applied in the former works as well and will be explained in chapter 3.

machines without the need to scan a calibration phantom during each imaging, §4.3.2. To perform FE simulation on the 3D reconstructed models, it is required to assign physical properties of bones to the models. But patients whose 3D bone models are requested, only provide x-ray images.

One of the feasible approaches for this purpose is attributing mechanical properties to the 3D models in the CT dataset using their provided CT scans. Then the most similar bone parts are found and their bone mass density (BMD) values are transferred into the new model. However, this method is faced with an obstacle which is lack of calibration images. To solve this problem, a method is proposed to calibrate previous scans of CT machines, §4.3.2. The solution originates from this view that instead of calibrating CT scans at each screening, the CT machine is calibrated once and the obtained relationships are used thereafter.

Chapter 2

3D reconstruction of skeletal structures

Overview

- **Novelty**: Introducing a method for creating 3D models from standard x-ray images.

- **Method**: Former works in the field of 3D reconstruction from 2D images are based on modifying a mean model obtained from all bones in the dataset. In this chapter, a new approach is suggested, §2.2.6. Reasons for performing each step with a special method are explained at the beginning of the sections before employing the method.

2.1   Introduction

In this chapter, a new method for building 3D models from standard x-ray images is presented. It consists of the same steps as former works but instead of modifying a mean model, it uses a best-matching selection criterion, §2.2.6. In the following, former works and their frequent technical words are studied, §2.1.1 and §2.1.2. Thereafter, the framework's steps are described and their results are shown, §2.2.2 to §2.2.8.

2.1.1   Terminology

In this part, often used technical words in the literature are defined. An interested reader can find more information in DESERNO (2011) and GONZALEZ & WOODS (2008).

Image: explained by a function $f(x, y)$ which describes brightness in spatial coordinates. Elements of image called pixel are entries of this matrix.

DICOM: an abbreviation for Digital Imaging and Communication in Medicine, defines a file format and a network communication protocol for handling, storing, printing and transmitting medical images. When an equipment supports DICOM standard, it means it can receive/send data from/to other equipments that support the DICOM standard.

X-ray: discovered by Wilhelm Conrad Roentgen in 1895, can be generated if an electron from a higher orbit jumps into an inner orbit. When x-ray passes through a material, amount of absorption depends on the photon energy and thickness of

the material while every material has a unique absorption coefficient.

DXA: Dual-energy x-ray absorptiometry is used to measure bone mineral density (BMD) by means of two x-ray beams with different energy loads.

CT and x-ray imaging: body part is imaged from a very limited viewpoints during x-ray imaging. In Computer Tomography (CT) by using a rotating angular gantry moving in a spiral path, more images are obtained and then analyzed to build a 3D view of the imaged body part.

AP view: an abbreviation for the Anterior-Posterior view, means that the x-ray source is placed in front of the patient and the detector is placed at the back.

Segmentation: means relevant information to the purpose of segmentation are extracted. To segment a part, labeling should be performed meaning pixels representing a relevant part are marked with the same tag.

Rigid registration: before comparing outlines of two bones, to evaluate the differences originate from different geometry and not from different positions in the space, input images are rigid registered which means translation, scaling and rotation effects are removed.

Smoothing: is performed to prepare surfaces for volume meshing by attenuating the edges. Through this approach, appearance of the model is improved that is useful during comparing outline of bones and also during the mesh generation.

2.1.2 Current Methods for Creating 3D Models From 2D Images

A series of publications from one group in the field of building a 3D model from 2D images are ZHENG ET AL. (2009), SCHUMANN ET AL. (2010), ZHENG (2010), SCHUMANN ET AL. (2013b), SCHUMANN ET AL. (2013a). The mathematical idea in these works are the same and they applied the method on different parts of the human body (ZHENG ET AL., 2009; ZHENG, 2010), changed the view point to the problem (SCHUMANN ET AL., 2010, 2013a) or used different mathematical functions (SCHUMANN ET AL., 2013b). Their approach was that first, point distributed models (PDM) of the bones in the dataset were produced. Then by using the principal component analysis (PCA) or the least square regression, a mean model was obtained, No. 3.

Afterwards, the 3D mean model was projected, No. 8, in a view which the new patient's image was provided. They did not mention the smoothing step; however, from the smooth surface of bones in their provided figures, it is concluded that they performed the smoothing, No. 6, as well. By accomplishing the scaling, rigid registration, comparison between projection of the mean model and the patient's x-ray image, and then carrying out a 2D-3D registration, No. 11, the mean model was modified and considered as the 3D model of the new patient's bone. The procedure to perform the 2D-3D registration in their work was measuring a distance in projection of the mean model and then scale it to the size of the patient's bone.

EHLKE ET AL. (2013) used the same approach while they considered distribution of density as well. To project the mean model before comparing with the patient's image, they proposed a method implemented in a parallel computing platform, CUDA, to make it possible to compute projections of the images faster. Their focus in this work was on presenting this algorithm and did not explain two critical issues, namely how to compare the projection with the patient's x-ray image and what to do after this comparison to improve the mean model and make it more similar to the x-ray image.

In this work, they used Bernstein density polynomial to calculate density values from CT scans and in their former work (HELLMICH ET AL., 2008) they had the following strategy: first translating voxel's coefficients of x-ray attenuation of a micro computer tomographic image into volume fractions of hydroxyapatite, collagen, and water.

For this purpose, they used an average rule for x-ray attenuation coefficients and a composition law for extracellular bone matrix obtained from two published sources (VUONG & HELLMICH, 2011; DEJACO ET AL., 2012). Afterwards they used a multiscale approach to calculate the elastic properties in macro scale. In other words, they proposed a method to calculate voxel-specific elastic properties by converting the x-ray attenuation information based on the fundamentals of x-ray physics. They claimed that it is applicable to medical CT scans and x-ray images as well.

One of the latest work in the area of building 2D patient-specific finite element

modeling from a patient's DXA image with the help of a dataset is SARKALKAN ET AL. (2014a). In contrast to the former works, they could manage to perform it in an automated framework but did not report the error of the material mapping. The same lack of report goes to the recent work by VÄÄNÄNEN ET AL. (2015) which used DXA images to build the 3D patients' specific bone models.

2.2   Method and Results

In this part, first, information about the CT dataset of the work is presented and then the utilized tools for implementation of the framework are introduced and their results are displayed. The procedure to perform these steps in the software can be found in the appendix A.

2.2.1   Materials

Our dataset comprised 80 sets of pelvis and femur CT images of patients of different ethnicities (based on names of Arab, German, Russian and Turkish origin), genders, and ages, with some including implants. Forty-five sets of images of the dataset were then selected for this study by a hip joint surgeon as normal bones with no skeletal pathology. Thirty of collected models were randomly set as the training set, No. 1, 18 females bone and 12 males aged 18-88 years (avg., SD: 52.19, 10.38), and the rest 15 femurs composed the test group, No. 10, 9 females

bone and 6 males aged 20- 78 years (avg., SD: 53.78, 9.61).

2.2.2   Segmentation, Step 2 of the Framework

To acquire a 3D model from CT scans of a patient, the outline of bone in each CT slice is required to be segmented. Gold models from CT scans are provided by manual segmentation (KAINMUELLER, 2015). This approach is applied in this work as well. For the images that the bone outline are clearly distinguishable, such as the outline after projecting in No. 8, a semi-automatic level set which has been applied successfully by YUSHKEVICH ET AL. (2006) is utilized. An automatic segmentation (SEIM ET AL., 2008) is not applied as its development is a time consuming task without giving any extra benefit to the purpose, introducing a best-matching selection criterion instead of the statistical approaches.

To explain the mathematics of the method (LI ET AL., 2010; OSHER & SETHIAN, 1988), imagine Γ in $\mathcal{R}^n$ of codimension one bounds an open region Ω. A smooth function $\Phi(\boldsymbol{x}, t)$, called level set function (LSF), is defined as

$$\begin{cases} \Phi(\boldsymbol{x}, t) > 0 & \boldsymbol{x} \in \Omega \\ \Phi(\boldsymbol{x}, t) < 0 & \boldsymbol{x} \in \bar{\Omega} \\ \Phi(\boldsymbol{x}, t) = 0 & \boldsymbol{x} = \Gamma(t) \end{cases} , \qquad (2.1)$$

where the third state is called zero level set and $\boldsymbol{x} = \boldsymbol{x}(x_1, x_2, \ldots, x_n) \in \mathcal{R}^n$ and t represent position and time, respectively. To analyze the motion of Γ, the

Φ values are convected with a velocity $\boldsymbol{v}$ as

$$\frac{\partial \Phi}{\partial t} + \boldsymbol{v} \cdot \nabla \Phi = 0 \qquad , \tag{2.2}$$

where $\boldsymbol{v}$ represents the velocity on the interface. Using the normalized velocity,

$$v_N = \boldsymbol{v} \cdot \frac{\nabla \Phi}{|\nabla \Phi|} \qquad , \tag{2.3}$$

equation 2.2 is rewritten as

$$\frac{\partial \Phi}{\partial t} + v_N |\nabla \Phi| = 0 \qquad . \tag{2.4}$$

Although the main focus is on the zero level set of the LSF and not on the LSF

itself, a distance condition is set for the LSF to keep the level set evolution stable.

This condition is expressed by $|\nabla \Phi| = 1$. To meet this condition, one approach is

to reinitialize the LSF after each period as a signed distance function. However,

it can cause incorrect movement of the zero level set from the expected position.

Also, lack of a general answer to the questions when and how the reinitializa-

tion should be performed, encourages looking for methods without the need for

reinitialization. An approach which employs a LSF that intrinsically satisfy the

unity of the signed distance function is: first an energy function on Φ is defined

$$E(\Phi) = \mu R_P(\Phi) + E_{ext}(\Phi) \qquad , \tag{2.5}$$

where the regularization function is described by

$$R_P(\Phi) = \int_\Omega P(|\nabla\Phi|)d\boldsymbol{x} \qquad (2.6)$$

and P is a potential function with the below specific construction

$$P(s) = \begin{cases} \frac{1}{(2\pi)^2}(1 - \cos(2\pi s)) & s \leq 1 \\ \frac{1}{2}(s-1)^2 & s \geq 1 \end{cases} \qquad (2.7)$$

E_{ext} in equation 2.5 is an energy function containing the minimum value when the desired area is segmented, i.e., zero level set is placed on the desired object. Derivative of equation 2.5 results in

$$\frac{\partial E}{\partial \Phi} = \mu\frac{\partial R_P}{\partial \Phi} + \frac{\partial E_{ext}}{\partial \Phi} \qquad (2.8)$$

From calculus of variation, solution of

$$\frac{\partial \Phi}{\partial t} = -\frac{E(\Phi)}{\partial \Phi} \qquad (2.9)$$

gives the minimum of the energy functional $E(\Phi)$. The derivative of the function $R_P(\Phi)$ is

$$\frac{\partial R_P}{\partial \Phi} = -div(d_P(|\nabla\Phi|)\nabla\Phi) \qquad , \qquad (2.10)$$

where the function d_P is defined as

$$d_P(s) = \frac{P'(s)}{s} \qquad (2.11)$$

and

$$P'(s) = \begin{cases} \frac{1}{2\pi} \sin(2\pi s) & s \leq 1 \\[2mm] (s-1) & s \geq 1 \end{cases} . \qquad (2.12)$$

Combination of equations 2.9 and 2.8 results in

$$\frac{\partial \Phi}{\partial t} = -\mu \frac{\partial R_P}{\partial \Phi} - \frac{\partial E_{ext}}{\partial \Phi} \qquad . \qquad (2.13)$$

By substituting equation 2.10 in this equation, the evolution equality is obtained

$$\frac{\partial \Phi}{\partial t} = \mu \, div(dp(|\nabla \Phi|)\nabla \Phi) - \frac{\partial E_{ext}}{\partial \Phi} \qquad , \qquad (2.14)$$

where the external energy is

$$E_{ext} = \lambda L_g(\Phi) + \alpha A_g(\Phi) \qquad . \qquad (2.15)$$

In this equation, α and λ are real numbers where $\lambda > 0$,

$$L_g(\Phi) = \int_\Omega g\delta(\Phi)|\nabla \Phi| d\boldsymbol{x} \qquad (2.16)$$

and

$$A_g(\Phi) = \int_\Omega gH(-\Phi)d\boldsymbol{x} \qquad , \qquad (2.17)$$

where δ is the Dirac delta function, H is the Heaviside function and g is an edge

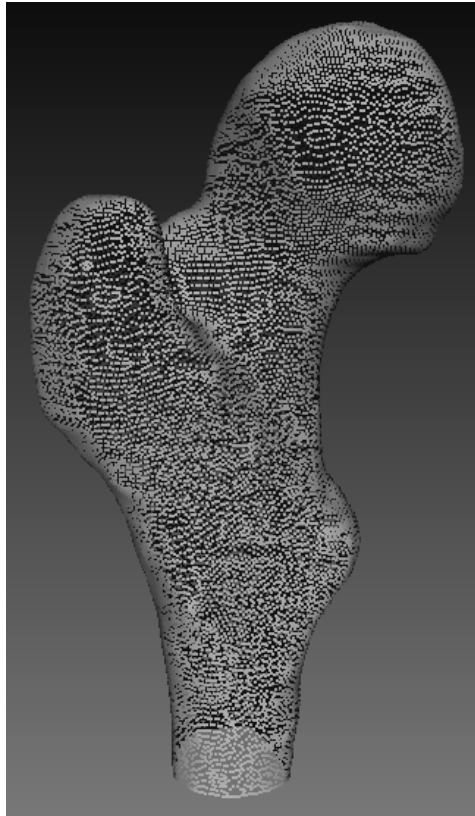indicator function that takes small values at boundaries of the object.

Figure 2.1: A point cloud obtained after segmenting CT slices of a femur.

Practically, smoothened Dirac delta and Heaviside functions are used which are

defined as

$$\delta_\epsilon(\boldsymbol{x}) = \begin{cases} \frac{1}{2\epsilon}\left[1 + cos(\frac{\pi\boldsymbol{x}}{\epsilon})\right] & |\boldsymbol{x}| \le \epsilon \\ 0 & \text{otherwise} \end{cases} \qquad (2.18)$$

and

$$H_\epsilon(\boldsymbol{x}) = \begin{cases} \frac{1}{2\epsilon}\left(1 + \frac{\boldsymbol{x}}{\epsilon} + \frac{1}{\pi}\sin(\frac{\pi\boldsymbol{x}}{\epsilon})\right) & |\boldsymbol{x}| \leq \epsilon \\[2ex] 1 & |\boldsymbol{x}| > \epsilon \\[2ex] 0 & |\boldsymbol{x}| < -\epsilon \end{cases} \qquad . \qquad (2.19)$$

In case of applying a manual segmentation, the itk-Snap software (YUSHKEVICH ET AL., 2006) is employed and the procedure is explained in appendix A.1. After performing the segmentation, a point cloud is obtained, step 3 (Fig. 2.1), on which a surface is reconstructed in the next step.

2.2.3   Surface Reconstruction, Step 4 of the Framework

Reconstructing 3D surfaces from point clouds means providing a mesh on the point samples. Previous works in this field did not report their method for this step. Therefore, it is not possible to select a method based on their obtained results. In general, three approaches can be applied for this purpose from which the two are: methods that are based on combinatorial structures such as Delaunay triangulation (KOLLURI ET AL., 2004; BOISSONNAT, 1984) and Voronoi diagrams (AMENTA ET AL., 2001, 1998), and those that reconstruct an approximating surface directly (SHEN ET AL., 2004).

The third approach is the Poisson method that is applied in this work because it is more stable than the others in presence of data noises (KAZHDAN & HOPPE,

2013). The method can be expressed as a solution of a Poisson equation using an implicit function framework. The main part of the method is the computation of a 3D indicator function χ, i.e., inside points are set as 1 and outside points 0. As the indicator function is constant almost everywhere, its gradient is zero almost everywhere except at points near the surface which is equal to the surface normals[1]. So the problem changes to find the indicator function, χ_M, of solid M whose gradient equals to the vector field $\boldsymbol{N}_{\partial M}$[2] defined by the sample points on the surface ∂M, i.e.

$$\nabla \chi_M = \boldsymbol{N}_{\partial M} \qquad . \tag{2.20}$$

By applying the divergence operator, equation 2.20 transforms to

$$\Delta \chi_M = \nabla . \boldsymbol{N}_{\partial M} \tag{2.21}$$

which is a Poisson equation and the obtained χ_M represents the surface. To avoid unbounded values during the computation of the gradient of the indicator function, as it is a piecewise constant function, it is first smoothened and then a relationship between this smoothened function and the surface normal field is formulated. For this purpose equation 2.20 is rewritten as

$$\nabla (\chi_M * F)(q) = \int_{\partial M} F_P(q) \, \boldsymbol{N}_{\partial M}(P) \, dP \qquad , \tag{2.22}$$

---

[1]They are computed by considering neighbors of a vertex, creating a local surface there, and calculating the normal vector to that surface.

[2]The same function was defined in the description of the level set function but in this case, the right hand side of the equation, $\boldsymbol{N}_{\partial M}$, is known.

where $*$ represents the convolution operation, F_q is the smoothing filter, and P is a point on the boundary. Equation 2.22 means that the gradient of the smoothened indicator function is equal to the vector field obtained by smoothening the surface normal field which is approximated by the summation of smoothened input point sets' normals times by their corresponding areas (KAZHDAN & HOPPE, 2013).
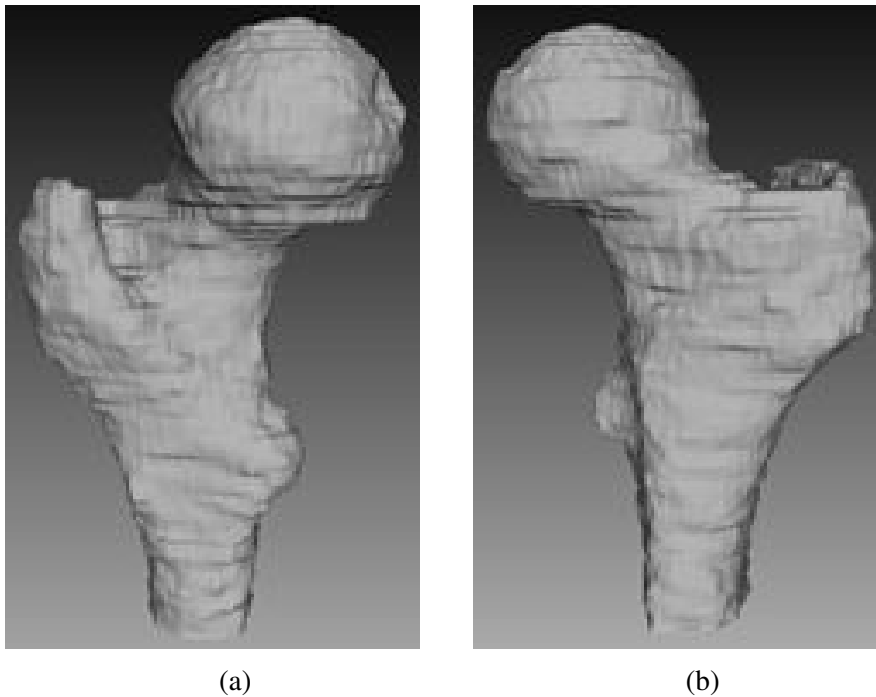

(a)   (b)

Figure 2.2: Two views of the built surface, No. 5, on the acquired point cloud, Fig. 2.1, using the Poisson surface reconstruction method.

Applying this method using the MeshLab software (CIGNONI ET AL., 1998), explained in the appendix A.2, results in step 5 of the framework, Fig. 2.2, a surface model that consists of 60,632 faces and contains no holes although it is not smooth.

2.2.4   Smoothing, Step 6 of the Framework

As it is displayed in Fig. 2.2, the built surface on the point cloud is not smooth which is required for meshing and comparing the outlines. Previous works did not report their method for this step (TADDEI ET AL., 2006; ZHENG ET AL., 2009; SCHUMANN ET AL., 2013a; SARKALKAN ET AL., 2014a; VÄÄNÄNEN ET AL., 2015). Therefore, it is not possible to select a method based on their obtained results. The Taubin filtering was selected in this work because it was specifically developed for medical images to be able to handle their large number of vertices. Other existing algorithms (MORETON & SÉQUIN, 1992; HALSTEAD ET AL., 1993) for this purpose are computationally more expensive (TAUBIN, 1995).

Smoothening a closed curve or surface by the Taubin filtering means removing noises from the coordinate signals. Its mathematical framework can be explained by considering a function defined on a regular polygon of n vertices, $\boldsymbol{x} = (x_1, ..., x_n)^T$, where x_i represents the value of the signal at the vertex i of the polygon. The discrete Laplacian of $\boldsymbol{x}$ for node j on the neighbor of node i, i^*, is defined as

$$\delta x_i = \sum_{j \in i^*} w_{ij}(x_j - x_i) \qquad , \qquad (2.23)$$

where w_{ij} is equal to the inverse number of neighbors of the vertex x_i. Then, a

matrix $\boldsymbol{K}$ is defined by $\boldsymbol{K} = \boldsymbol{I} - \boldsymbol{W}$, where elements of $\boldsymbol{W}$ are

$$
\begin{cases}
w_{ij} = 1 & j \text{ is a neighbor of } i \\
w_{ij} = 0 & \text{otherwise}
\end{cases}
\tag{2.24}
$$

and a signal $\boldsymbol{x}$ is described by

$$
\boldsymbol{x} = \sum_{i=1}^{n} \xi_i \, \boldsymbol{u}_i \qquad , \tag{2.25}
$$

where $\boldsymbol{u}_i$ is an eigenvector from the linear decomposition of the signal. A

smoothened signal is attained from

$$
\boldsymbol{y} = \sum_{i=1}^{n} \xi_i \, f(k_i) \, \boldsymbol{u}_i \qquad , \tag{2.26}
$$

where k_i is an eigenvalue of matrix $\boldsymbol{K}$, the polynomial f is defined as

$$
f(k_i) = (1 - \lambda k_i)(1 - \mu k_i) \tag{2.27}
$$

and the two coefficients are given as input considering the following limitations:

$\lambda > 0$ and $\mu < -\lambda$. By this definition, when iteration numbers N increases

$$
\begin{cases}
f_{k_i}^{N} \approx 1 & k_i \approx 0 \\
f_{k_i}^{N} \approx 0 & k_i \approx 2
\end{cases}
. \tag{2.28}
$$

As it is shown that eigenvalues of matrix K are positive and less-equal to two (KAZHDAN & HOPPE, 2013), it can be seen from equation 2.28 that frequencies with large eigenvalues are removed from the smoothened signal y, equation 2.26. By removing these frequencies a smoothened image is obtained with the same number of vertices and faces.
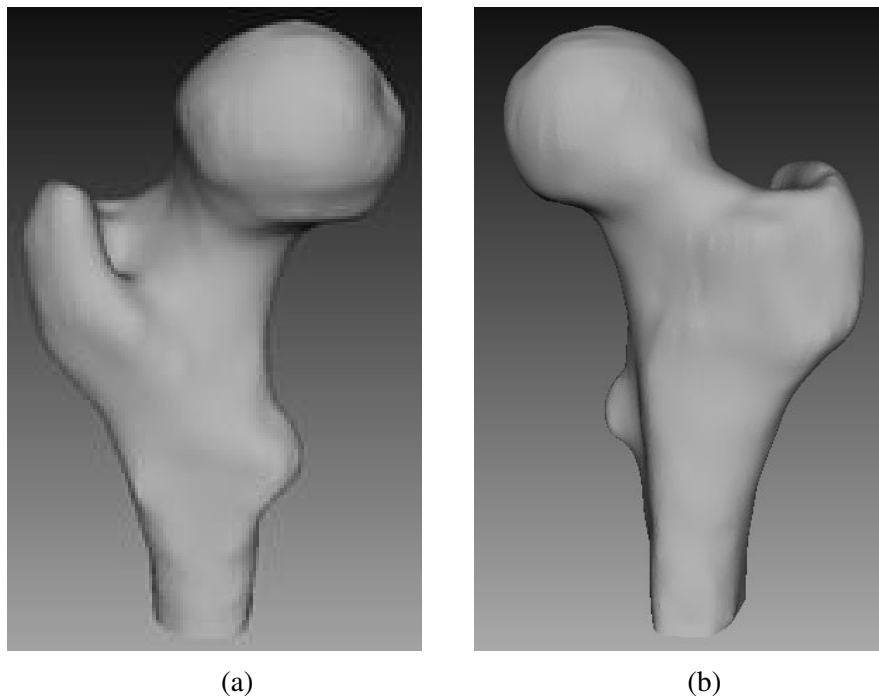

(a)   (b)

Figure 2.3: The two surface bone models in the previous step after performing the Taubin filtering on them.

Applying this method implemented in the MeshLab software (CIGNONI ET AL., 1998), described in appendix A.2, results in a smoothened model, No. 7, of the unsmoothed bone, Fig. 2.3. As it can be seen, the edges in the Fig. 2.2 have been removed and the outline of bones can be compared together after projecting the model. The model consists of 30,401 vertices and 60,632 faces that are similar to the model's before the smoothing.

2.2.5 Projection, Step 8 of the Framework

To compare the outline of bones in the dataset with the new patient's x-ray image, No.10, they are projected in the AP view. For that purpose, the user places the model in the AP view position before the projecting, a method that is applied during DXA imaging[3].
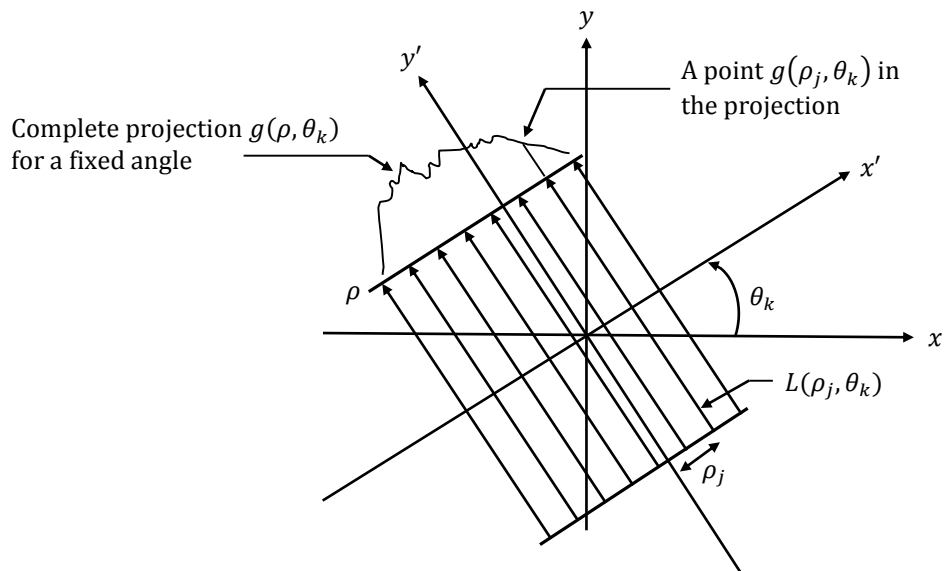

Figure 2.4: Depiction of the emitted ray $L(\rho_j, \theta_k)$ at the displayed angle and radius to compute the equation 2.30. Photo credit: reproduced from GONZALEZ & WOODS (2008).

The projecting process is that a virtual x-ray source in front of the model and a flat detector at the back of the model are placed. The distances are retrieved from the meta data of the CT scans. By describing a line in the Cartesian coordinates

---

[3]For instance in the HOLOGIC DXA machines, a hip positioning fixture is provided besides the imaging machine. When the femur is going to be scanned, the patient is requested to place his foot on the fixture. Its special V shape causes the femur to be placed in a AP view. In some cases, after imaging it is seen that the femur still needed to be rotated inward or outward. In such a case, the radiologist repeats the scan after modifying the patient's position.

as

$$x \cos \theta + y \sin \theta = \rho \qquad , \qquad (2.29)$$

where ρ and θ are shown in Fig. 2.4. One point of projection of the image $f(x,y)$
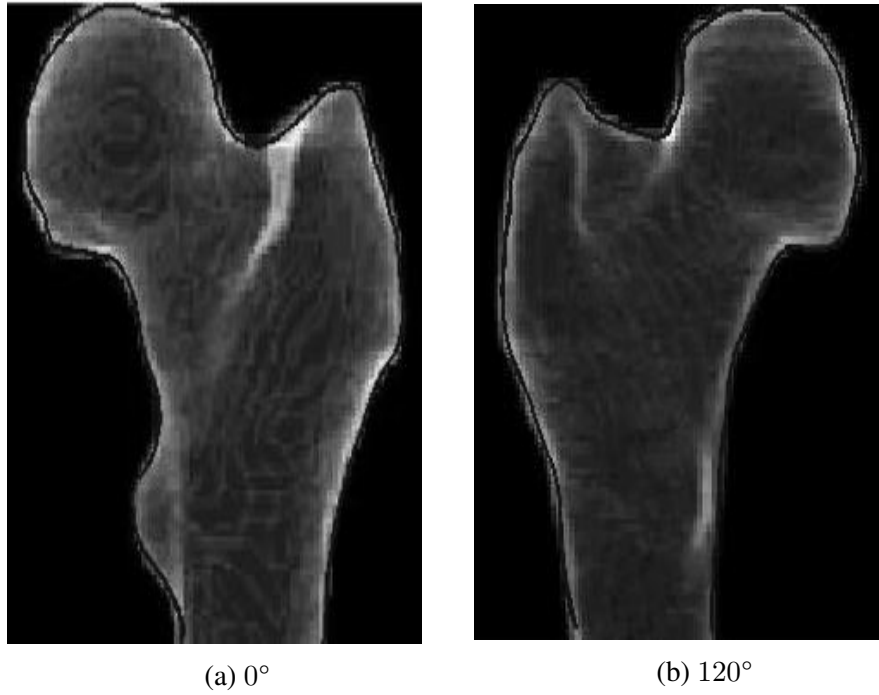

(a) 0°
(b) 120°

Figure 2.5: Projections of the 3D built bone model in two views, No. 9. The outlines were captured using the level set segmentation method, §2.2.2.

is modeled by parallel ray beams as

$$g(\rho_j, \theta_k) = \int_{-\infty}^{\infty} \int_{-\infty}^{\infty} f(x, y)\, \delta(x \cos \theta_k + y \sin \theta_k - \rho_j)\, dx\, dy \qquad , \quad (2.30)$$

where the angle θ_k and the length ρ_j are defined in Fig. 2.4. Allowing ρ to vary while θ is fixed, yields a total projection of the body part f(x,y). After projection of the smoothened bone model, Fig. 2.5, its outline is detected using the semi-automatic level set method.

2.2.6   Registration and Comparison the Outlines, Step 11 of the Framework

In this section, the best-matching selection criterion is introduced. It consists of the below steps:

- The bone is divided into some areas and one part is determined as the most important one during the reconstruction[4]. For instance, a femur is considered in four areas, namely the head, the neck, the trochanter, and the shaft.

- Outlines of the models in the dataset are compared with the new patient's as

  1- The 3D models are scaled using the MeshLab software. The scale ratio equals to the ratio of the most important part measured in the new patient's outline and the patients' in the dataset.

  2- To remove the translational and rotational effects, the point sets are registered using the Iterative Closest Point (ICP) algorithm (BESL & MCKAY, 1992). This method and also the criterion used in the next step were selected as they were recommended by the ZHENG ET AL. (2009) and ZHENG (2010). Subjects of the two studies were similar to that of the present work. They examined various approaches for

---

[4]Determining, e.g., where the neck starts and where it ends is based on the radiologist's diagnosis. This is the procedure in the DXA software as well, i.e., the radiologist puts the box of the neck area where he considers as the correct position.

registering the models and the measurement criterion and concluded

that the ICP algorithm and the Hausdorff criterion resulted in satisfy-

ing results. To describe mathematics of registration, the transforma-

tion of pixel coordinates in the original image (v, w) is expressed by[5]

$$[x, y, 1] = [v, w, 1] \, \boldsymbol{T} \qquad , \qquad (2.31)$$

where (x, y) represents the corresponding pixel coordinates in the

transformed image. To rotate the image in θ degree the transforma-

tion matrix is organized as

$$\boldsymbol{T} = \begin{bmatrix} \cos\theta & \sin\theta & 0 \\ -\sin\theta & \cos\theta & 0 \\ 0 & 0 & 1 \end{bmatrix} \qquad . \qquad (2.32)$$

To map two images to each other using the translation transformation,

two parameters, t_x and t_y, are searched to form the transformation

matrix as

$$\boldsymbol{T} = \begin{bmatrix} 1 & 0 & 0 \\ 0 & 1 & 0 \\ t_x & t_y & 1 \end{bmatrix} \qquad . \qquad (2.33)$$

The ICP algorithm iteratively revises the translation and the rotation

parameters up to satisfying a stopping criterion, i.e., a determined

---

[5]The $\boldsymbol{T}$ matrix does not need to be transposed.

limitation by the user for the maximum least square distance between models after each iteration. Below items are the steps of the algorithm:

I) The closest point in the reference image is searched for each point of the target image while the Euclidean distance between the two points, $r_i = r_{ji}$, $j = 1, 2, 3$ and $i = 1, 2$, is defined by

$$d(\boldsymbol{r_1}, \boldsymbol{r_2}) = \sqrt{\sum_{j=1}^{3} (r_{j1} - r_{j2})^2} \qquad . \qquad (2.34)$$

When A is a point set with N_a points denoted by a_k, equation 2.35 results in the distance between a point P and the point set A,

$$d(P, A) = \min d(P, a_k), \ k = 1, ..., N_a . \qquad (2.35)$$

II) The required parameters for the rotational and translational transformations are found by optimizing a mean squared error cost function to align each pair of points found in the previous step. This procedure between two point sets is defined by

$$F(\boldsymbol{R}, \boldsymbol{t}) = \min \sum f(d(\boldsymbol{R}_{a_k} + \boldsymbol{t}, X)) \qquad , \qquad (2.36)$$

while $\boldsymbol{R}$ is a rotation matrix ($\boldsymbol{R}^T \boldsymbol{R} = \boldsymbol{I}$, $det(\boldsymbol{R}) = 1$), $\boldsymbol{t}$ is a translation vector, and a_k are members of A as defined in (I). The point set A and X respectively represent the target and reference

images.

III) A new target point cloud[6] is obtained by transforming the target image using the calculated transformation parameters obtained in the former step.

3- The Hausdorff criterion (HAUSDORFF & WETS, 1998) is applied to quantify similarity between two point clouds by calculating the distances between corresponding points. The average of all distances is reported as a number and the smaller it is, the more similar the models are to each other. To measure the Hausdorff distance between two models A and B containing respectively P and Q points, the following algorithm is performed for all points of the model A, $I^A = \left\{ I_i^A, i = 1, ..., P \right\}$:

I) Points of the model B that are in the vicinity of I_i^A in a radius defined by the user as input, known as the kernel size, are determined[7]:

$$\Omega^B = \left\{ \Omega_j^B, \ j = 1, ..., M \right\} \qquad . \qquad (2.37)$$

II) The distance between point I_i^A with each of Ω_j^B is calculated (in the Cartesian coordination, it is

---

[6]After reconstructing the surfaces, again they are referred to as point clouds because when two surfaces are compared, distances between their corresponding points are calculated. Also, when a surface is smoothened by the Taubin filtering, position of its points are regulated. In other words, point cloud and surface are two equivalent words in this context and the operations that are performed on the surfaces, actually act on the point clouds.

[7]The distance between each point of model B and I_i^A is measured and if it is less than the kernel size, it means that the point is a neighbor of I_i^A.

known as the Euclidean distance which is equal to

$\sqrt{(x_{I_i^A} - x_{\Omega_j^B})^2 + (y_{I_i^A} - y_{\Omega_j^B})^2 + (z_{I_i^A} - z_{\Omega_j^B})^2)}$ and max-

imum amount is then considered as the distance between the

models A and B at point i,

$$d_i^{AB} = \max \left| I_i^A - \Omega_j^B \right|, \; j = 1,...,M \qquad . \qquad (2.38)$$

III) Distance between the models A and B is then defined as the

average of all d_i^{AB}, i.e.

$$D^{AB} = mean \left(d_i^{AB}, \; i = 1,...P \right) \qquad . \qquad (2.39)$$

- The model which results in the minimum Hausdorff distance is considered

as the 3D bone model of the new patient.

Therefore, to reconstruct, e.g., a femur from its 2D image, referred to as new

femur in the following, the procedure is that

1. One part is considered as the most important one that in this example, the

neck is selected.

2. Ratios between ND of models[8] in the dataset with ND of the new femur

are calculated and the 3D models are then scaled.

3. The new models are projected, their outlines are obtained, and compared

---

[8]It is measured on the AP outlines as shown in the Fig. 2.6.

with the new femur's outline. A 3D model with the minimum Hausdorff

distance is selected as the 3D model of the new femur.
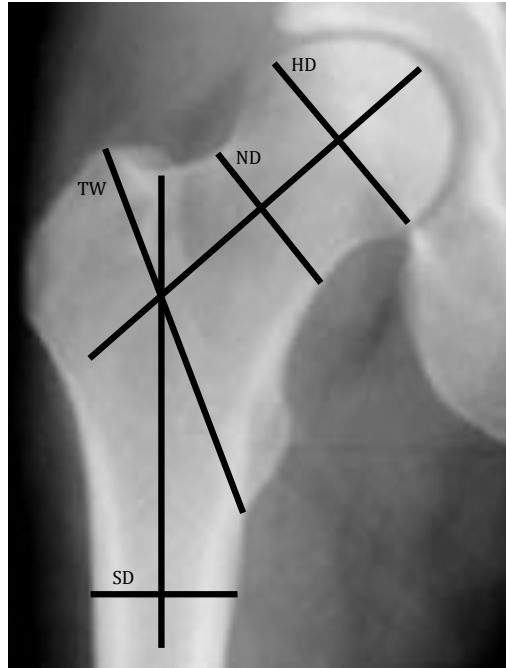
Figure 2.6: Geometrical parameters measured on a AP view of the femur to scale the patient's femur model. The TW line connects the highest point of the greater trochanter to the lowest point of the lesser trochanter. The HD represents the largest diameter in the femur head and the ND shows the diameter of the middle section in the neck area. The SD is considered $2\,\text{cm}$ below the lesser trochanter. Photo credit: reproduced from THEVENOT ET AL. (2013).

2.2.7   Finite Element Simulation on the Created Models

In the Finite Element analysis (FEA), an arbitrary body, Fig. 2.7, is approximated

by an assemblage of discrete finite elements interconnected at nodal points on

the element boundaries. The method can be applied to analyze both linear and

nonlinear problems and in the following an introduction to the linear analysis of

solids and structures is presented. The main nonlinearity in solid mechanics are

classified into five types (WRIGGERS, 2008), namely
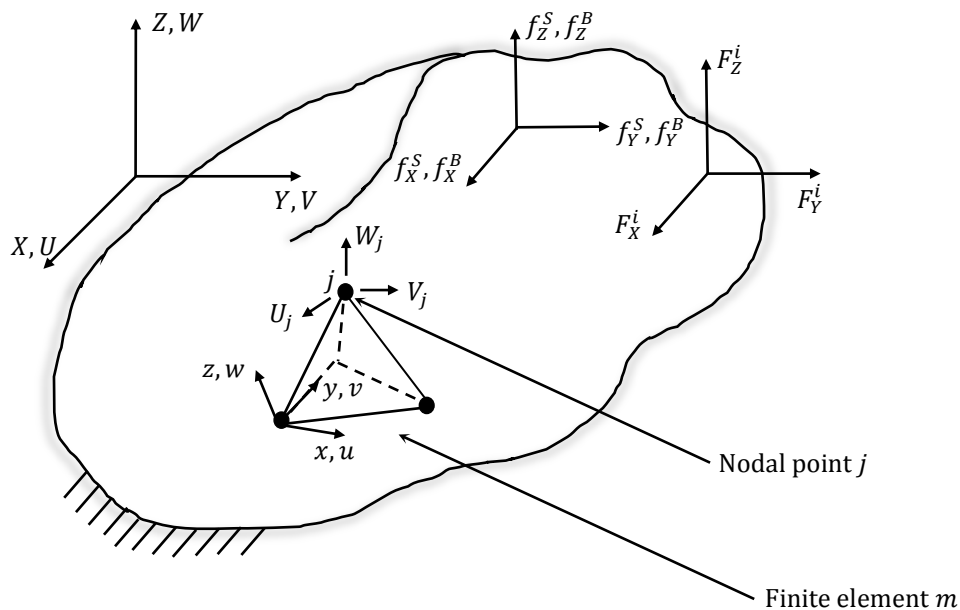
Figure 2.7: A general three-dimensional body with a tetrahedral finite element. Photo credit: reproduced from BATHE (2002).

- **Geometrical nonlinearity** in structural elements like as cables where strains are small but displacements and rotations are large.

- **Deformations nonlinearity** where both displacements and strains are large such as in a tyre.

- **Physical nonlinearity** originates from the material nonlinearity like as the concrete and soil.

- **Nonlinear boundary condition** occurs where a deformation dependent loading or the contact between surfaces are present.

- **Instability or coupled problem** like what comes along with necking or problems in which mechanical stresses, heat generation and conduction have to be coupled.

that in this work, none of them occurred, the simulated material is a linear elastic material, the loads are simulated statically, geometry does not have large displacement, and no nonlinear boundary condition or coupled problems are the matter of the case. To introduce a formulation of the displacement-based finite element method (BATHE, 2002), the 3D body displayed in Fig. 2.7 is considered subjected to concentrated forces F_x^i, F_y^i, and F_z^i at point i, body forces f_x^b, f_y^b, and f_z^b, and surface forces f_x^s, f_y^s, and f_z^s. The starting point in the FE analysis is the principal of virtual displacement (PVD):

$$\int_V \overline{\epsilon}^T \boldsymbol{\tau} dV = \int_V \overline{\boldsymbol{U}}^T \boldsymbol{f}^B dV + \int_S \overline{\boldsymbol{U}}^{S^T} \boldsymbol{f}^S S + \sum_i \overline{\boldsymbol{U}}^{i^T} \boldsymbol{F}_c^i \qquad , \qquad (2.40)$$

where

$$\overline{\boldsymbol{U}}^T = [\overline{U}\ \overline{V}\ \overline{W}]$$

$$\overline{\boldsymbol{\epsilon}}^T = [\overline{\epsilon}_{XX}\ \overline{\epsilon}_{YY}\ \overline{\epsilon}_{ZZ}\ \overline{\gamma}_{XY}\ \overline{\gamma}_{YZ}\ \overline{\gamma}_{ZX}] \qquad (2.41)$$

$$\boldsymbol{\tau}^T = [\tau_{XX}\ \tau_{YY}\ \tau_{ZZ}\ \tau_{XY}\ \tau_{YZ}\ \tau_{ZX}] \qquad .$$

The first three normal strain terms are computed by

$$\epsilon_{XX} = \frac{\partial U}{\partial X};\ \ \epsilon_{YY} = \frac{\partial V}{\partial Y};\ \ \epsilon_{ZZ} = \frac{\partial W}{\partial Z} \qquad (2.42)$$

and the next shear strain terms are calculated by

$$\gamma_{XY} = \frac{\partial U}{\partial Y} + \frac{\partial V}{\partial X};\ \ \ \gamma_{YZ} = \frac{\partial V}{\partial Z} + \frac{\partial W}{\partial Y};\ \ \ \gamma_{XZ} = \frac{\partial W}{\partial X} + \frac{\partial U}{\partial Z}\ . \qquad (2.43)$$

The corresponding stresses to ϵ are

$$\boldsymbol{\tau^T} = \begin{bmatrix} \tau_{XX} & \tau_{YY} & \tau_{ZZ} & \tau_{XY} & \tau_{YZ} & \tau_{ZX} \end{bmatrix} \qquad , \qquad (2.44)$$

where

$$\boldsymbol{\tau} = \boldsymbol{C}\boldsymbol{\epsilon} + \boldsymbol{\tau^I} \; . \qquad (2.45)$$

In equation 2.45, $\boldsymbol{C}$ is the stress-strain material matrix and $\boldsymbol{\tau^I}$ denotes the given initial stresses. The PVD states that if a body is subjected to any arbitrary virtual displacement $\overline{U}$ which satisfies the displacement boundary condition, then the virtual work, i.e., all loads applied on the virtual displacements, done externally is equal to the virtual work done internally by the real stresses, $\boldsymbol{\tau}$, that are in equilibrium with the externally applied forces multiplied by the virtual strains, $\overline{\epsilon}$, corresponding to the virtual displacements.

In FEA, it is assumed that the virtual displacement of element m, $\overline{\boldsymbol{u}}^{(m)}_{(x,y,z)}$ including $\overline{u}, \overline{v}$, and $\overline{w}$, is equal to a displacement interpolation matrix $\boldsymbol{H}^{(m)}_{(x,y,z)}$ times a virtual nodal point displacement vector $\overline{\widehat{U}}^T$ shown in equation 2.46

$$\overline{\boldsymbol{u}}^{(m)}_{(x,y,z)} = \boldsymbol{H}^{(m)}_{(x,y,z)} \overline{\widehat{U}} \qquad , \qquad (2.46)$$

where

$$\widehat{\boldsymbol{U}}^T = \begin{bmatrix} U_1 V_1 W_1 & U_2 V_2 W_2 & U_N V_N W_N \end{bmatrix} \qquad (2.47)$$

and N denotes the number of the nodal points. In other words, equation 2.46

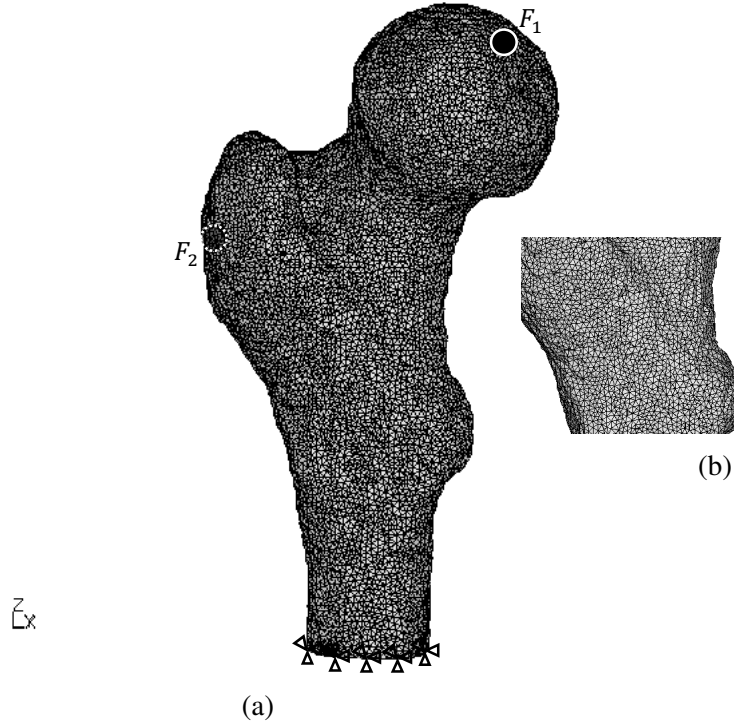describes the displacement in an element as a function of the nodal elements.

(a)

Figure 2.8: Displaying (a) the implemented boundary conditions, load forces, and (b) mesh quality of the reconstructed 3D femur model.

The strains are calculated as

$$\overline{\boldsymbol{\epsilon}}_{(x,y,z)}^{(m)} = \boldsymbol{B}_{(x,y,z)}^{(m)} \widehat{\overline{\boldsymbol{U}}} \qquad , \tag{2.48}$$

where $B_{(x,y,z)}^{(m)}$ is the strain interpolation matrix of the element m obtained by

differentiating columns of $H_{(x,y,z)}^{(m)}$. Rewriting PVD as a sum of integration over

the elements results in

$$\sum_m \int_{V^{(m)}} \bar{\boldsymbol{\epsilon}}^{(m)^T} \boldsymbol{\tau}^{(m)} dV^{(m)} = \sum_m \int_{V^{(m)}} \bar{\boldsymbol{u}}^{(m)^T} \boldsymbol{f}^{B^{(m)}} dV^{(m)}$$

$$+ \sum_m \int_{S^{(m)}} \bar{\boldsymbol{u}}^{S^{(m)^T}} \boldsymbol{f}^{S^{(m)}} dS^{(m)} \qquad (2.49)$$

$$+ \sum_i \bar{\boldsymbol{u}}^{i^T} \boldsymbol{F}_c^i \qquad\qquad .$$

By substituting equations 2.46 and 2.48 into the equation 2.49:

$$\overline{\widehat{\boldsymbol{U}}}^T \left\{ \sum_m \int_{V^{(m)}} \boldsymbol{B}^{(m)^T} \boldsymbol{C}^{(m)} \boldsymbol{B}^{(m)} dV^m \right\} \widehat{\boldsymbol{U}} = \overline{\widehat{\boldsymbol{U}}}^T \left\{ \sum_m \int_{V^{(m)}} \boldsymbol{H}^{(m)^T} \boldsymbol{f}^{B^{(m)}} dV^{(m)} \right.$$

$$+ \sum_m \int_{S^{(m)}} \boldsymbol{H}^{S^{(m)^T}} \boldsymbol{f}^{S^{(m)}} dS^{(m)}$$

$$- \sum_m \int_{V^{(m)}} \boldsymbol{B}^{(m)^T} \boldsymbol{\tau}^{I^{(m)}} dV^{(m)}$$

$$+ \boldsymbol{F}_c \}$$

$$(2.50)$$

that is the PVD equation in terms of the nodal point displacements and element

interpolation matrices which can be rewriting as in the following:

$$\boldsymbol{KU} = \boldsymbol{R} \qquad , \qquad\qquad (2.51)$$

where

$$\boldsymbol{R} = \boldsymbol{R}_B + \boldsymbol{R}_S + \boldsymbol{R}_I + \boldsymbol{R}_C$$

$$\boldsymbol{K} = \sum_m \int_{V^{(m)}} \boldsymbol{B}^{(m)^T} \boldsymbol{C}^{(m)} \boldsymbol{B}^{(m)} dV^m$$

$$\boldsymbol{R}_B = \sum_m \int_{V^{(m)}} \boldsymbol{H}^{(m)^T} \boldsymbol{f}^{B^{(m)}} dV^{(m)}$$

$$\boldsymbol{R}_S = \sum_m \int_{S^{(m)}} \boldsymbol{H}^{S^{(m)^T}} \boldsymbol{f}^{S^{(m)}} dS^{(m)} \qquad (2.52)$$

$$\boldsymbol{R}_I = \sum_m \int_{V^{(m)}} \boldsymbol{B}^{(m)^T} \boldsymbol{\tau}^{I^{(m)}} dV^{(m)}$$

$$\boldsymbol{R}_C = \boldsymbol{F}_c \qquad .$$

To evaluate the terms, in simple cases, analytical approach can be employed; however, in general, numerical integration is utilized for this purpose. In this case, if isoparametric finite element analysis is used, the displacement transformation matrix and the strain displacement interpolation matrix are functionals of the local element coordination r, s, and t. Thus the integrals change to

$$\boldsymbol{K} = \int \int \int \boldsymbol{B}^T \boldsymbol{C} \, \boldsymbol{B} \, det \boldsymbol{J} \, dr \, ds \, dt$$
$$= \int \int \int \boldsymbol{F}(r, s, t) \, dr \, ds \, dt \qquad , \qquad (2.53)$$

where $\boldsymbol{J}$ is the Jacobian transformation between the global and local coordinate axes. Using numerical integration, the stiffness matrix is computed by

$$\boldsymbol{K} = \sum \alpha_i \, \alpha_j \, \alpha_k \, \boldsymbol{F}(r_i, s_j, t_k) \qquad , \qquad (2.54)$$
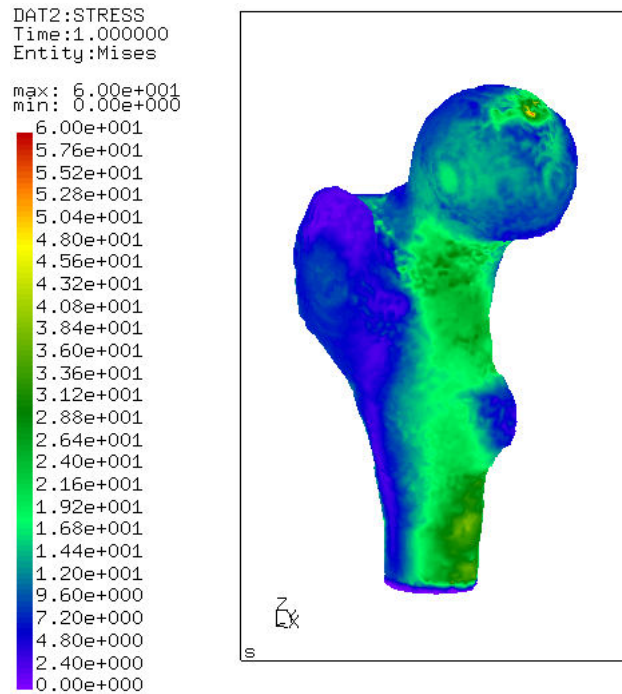
(a)
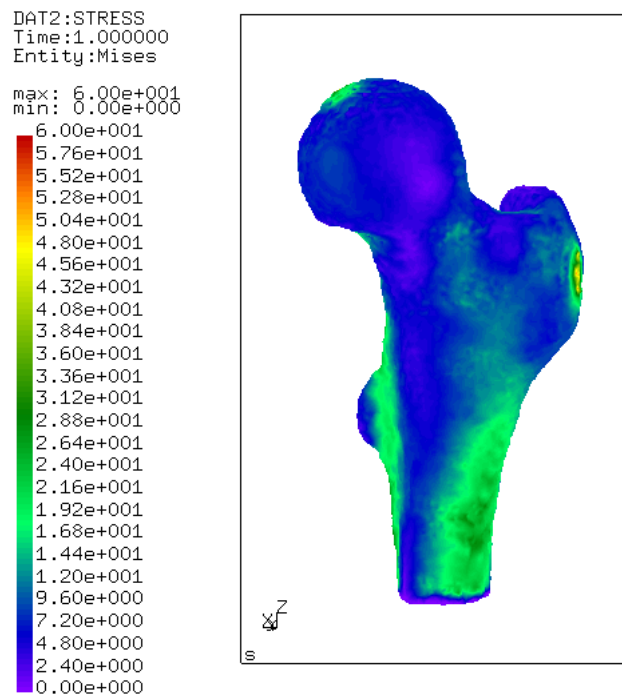
(b)

Figure 2.9: Stress field in MPa on the 3D model of the reconstructed femur undergone a linear finite element simulation.

where r_i, r_j, and r_k denote the integration points, and α_i, α_j, and α_k the corresponding weight coefficients. Equation 2.54 means function $\boldsymbol{F}(r_i, s_j, t_k)$ is evaluated at particular points i, j, and k in the element and then multiplied by attributed weights to those points. Different methods can be applied to choose these points but the Gauss numerical integration method is usually applied as the integration points are optimized by their locations in the interval and their corresponding weights, in contrast to the Newton-Cotes method that the points are equally placed in the interval and the weights can only be optimized.

Mechanical Properties and Boundary Conditions for the Simulation

The type of meshing, applied mechanical properties and boundary conditions implemented in this section are chosen from previous works who had the same subject to that of the present work and they reported their simulations' results were in agreement with the experiments' (HELLER ET AL., 2005; TADDEI ET AL., 2006; SPEIRS ET AL., 2007).

To perform the simulation on the built models, they were first meshed with tetrahedra elements using the Iso2mesh software (FANG & BOAS, 2009). The required commands for this purpose can be found in the appendix A.5. Physical properties of the bones including the Young's modulus and the Poisson's ratio were respectively set to $17\,\mathrm{MPa}$ and 0.3 (HELLER ET AL., 2005) and boundary conditions assigned as reported in SPEIRS ET AL. (2007). Nodes at the distal area were completely constrained and two vector forces $\boldsymbol{F_1} = (-490, 280, -1200)\,\mathrm{N}$

and $\boldsymbol{F_2} = (345, 150, 800)\,\text{N}$ acted on the model, Fig. 2.8.

To ensure that results are not dependent on the number of elements of the applied mesh while minimum number of elements are used, a mesh convergence study was performed. It was observed that the average of stress values in the section where the maximum stresses occurred was constant after meshing by 21,000 elements when number of elements increases from 3000 to 273,000. Results of the simulation using the FE software CalculiX are shown in the Fig. 2.8 and a description of the process is explained in the appendix A.6.

2.2.8   Application of the Framework on the Reconstruction of the Pelvis Bone

To investigate the application of the framework on the reconstruction of the pelvis bone, Fig. 2.10, it is enough to see whether the framework can build its gold model, No. 7. This is so because No. 8, projection, and No. 11, finding a similar model, can always be performed. Using the Hausdorff criterion, it is possible to measure the similarity between any two shapes. In any case, it results in a number that is used for classification of the similarity.

Defining characteristic lengths for the pelvis bone is possible as well, such as the introduced ones for the femur, Fig. 2.6. For instance, if the most important part is considered the acetabulum, its largest diameter can be considered for the scaling purpose though the reconstruction error might change when one defines

another characteristic length. Therefore, an appropriate topic for a study can be investigating how much selecting different characteristic lengths affect on the final reconstructed model.
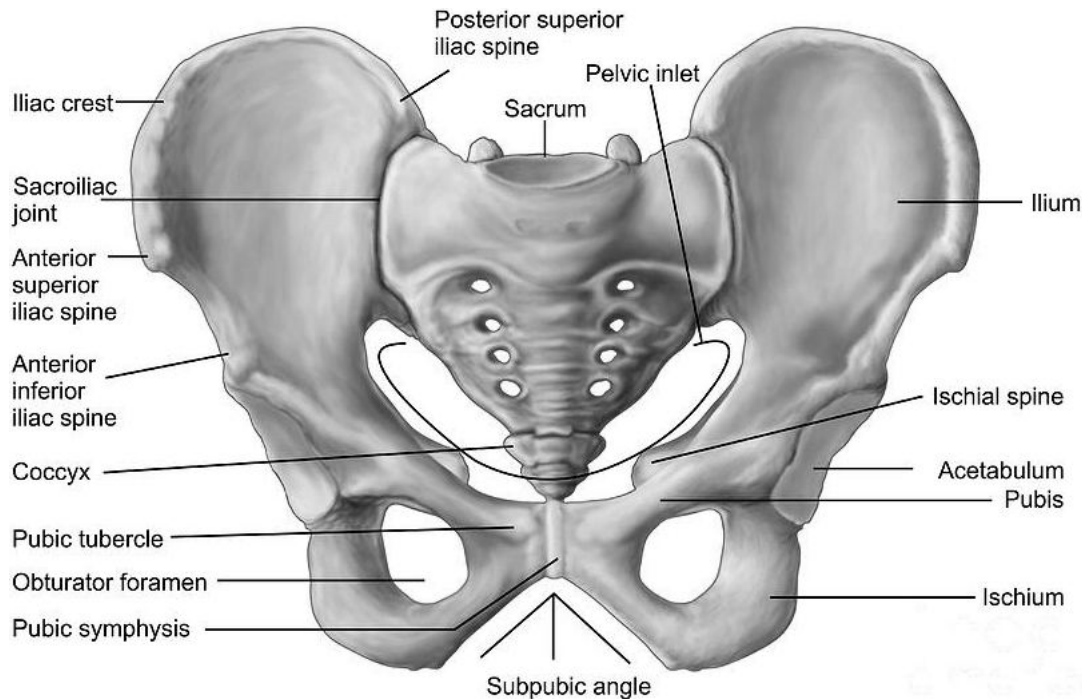
Figure 2.10: Displaying the bone structure of the pelvis. It consists of five major parts namely the sacrum, the illium, the ischium, the acetabulum, and the pubic bone. Source: https://singaporeosteopathy.com

A reconstructed pelvis bone model following No. 2, No. 4, and No. 6 after meshing by the Iso2mesh software is shown in Fig. 2.11. As the obtained model is a 3D model that can be utilized for further studies such as FE analysis, it is concluded that the method is capable of reconstructing a 3D model of the pelvis bone in a procedure similar to the one described for the femur reconstruction.

For that purpose, first, the most important part for the reconstruction is determined, e.g., the right acetabulum. Then ratios between the largest acetabulum's diameters of models in the dataset with the new pelvis's acetabulum's diameter

are calculated and the 3D models are then scaled. Afterwards, the new models are projected, their outlines are obtained, and compared with the new pelvis's outline. A 3D model with the minimum Hausdorff distance is selected as the 3D model of the new pelvis.
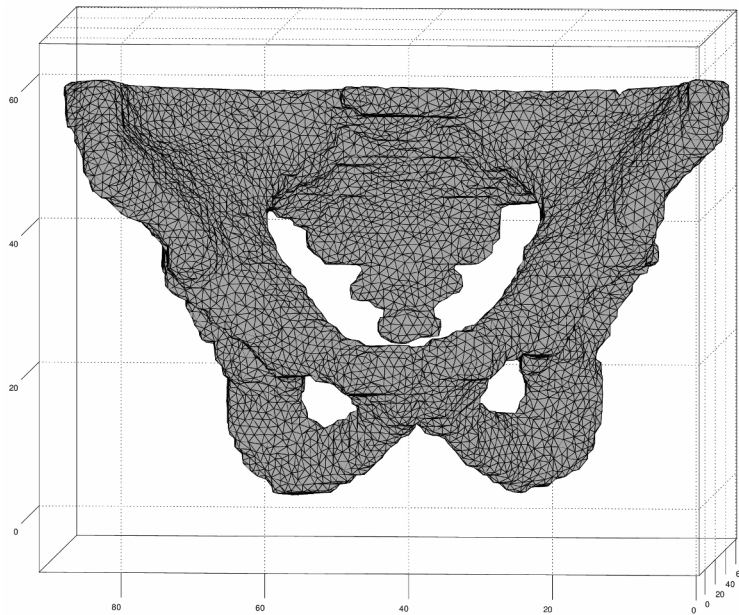
Figure 2.11: A reconstructed pelvis model after performing the segmentation, surface reconstruction and smoothing steps on CT scans of a patient in the dataset.

2.3   Discussion

One of the challenges in 3D reconstruction from x-ray images is that there is no information about the distance of the patient from the film required during the projection. ZHENG (2010) offered a distance of 150 mm; however, applying distances up to 600 mm is common in radiology centers depending on the cite of imaging and the required field of view.

In the literature there are three different methods to perform the scaling. One approach is using geometrical parameters and scaling the models according to the ratio between these parameters (ZHENG, 2010). The second method, proposed by DURRLEMAN ET AL. (2014), computes the distance of points of that shape from center of mass by

$$\sigma = \sqrt{\frac{1}{N}\sum_{i=1}^{N}||\boldsymbol{x}_i - \overline{\boldsymbol{x}}||^2} \quad , \tag{2.55}$$

where $\overline{\boldsymbol{x}}$ is calculated by

$$\overline{\boldsymbol{x}} = \frac{1}{N}\sum_{i=1}^{N}\boldsymbol{x}_i \tag{2.56}$$

for a typical point set $(\boldsymbol{x}_1, \ldots, \boldsymbol{x}_N)$. The scaling ratio between the two shapes is then equal to the ratio of their corresponding σ values. The third approach (DU ET AL.) is calculating the scaling for two sets of points, $\boldsymbol{x}_1$ and $\boldsymbol{x}_2$, by

$$s = \frac{trace(\boldsymbol{x}_2\,\boldsymbol{x}_1^T\,\boldsymbol{R}^T)}{trace(\boldsymbol{x}_1\,\boldsymbol{x}_1^T)} \quad , \tag{2.57}$$

where $\boldsymbol{R}$ is the rotation matrix computed by

$$\boldsymbol{R} = \boldsymbol{V}\,\boldsymbol{U}^T \quad . \tag{2.58}$$

In equation 2.58, $\boldsymbol{V}$ and $\boldsymbol{U}$ matrices are singular value decompositions (SVD) of the below matrix

$$\boldsymbol{M} = \boldsymbol{x}_1\,\boldsymbol{x}_2^T \quad . \tag{2.59}$$

All the works have reported satisfying results at the end regardless of the method that they employed in this step. Therefore, in this work the first method was applied as its subject of the study was similar to the present work's.

To quantify similarity among the models, one of the methods which is based on the distance between corresponding points, is the Hausdorff method that applied in this work. Another method suggested by (DURRLEMAN ET AL., 2014) and implemented in the Deformetrica software is that the distance between two meshes, S and S', is calculated by

$$
\begin{aligned}
d_W(S, S')^2 &= \|S - S'\|_{W*}^2 \\
&= \langle S, S \rangle_{W*} + \langle S', S' \rangle_{W*} - 2\langle S, S' \rangle_{W*}
\end{aligned}
\tag{2.60}
$$

that does not need vertex correspondences as the inner product reads

$$
\langle S, S' \rangle_{W*} = \sum_p \sum_q k^W(c_p, c_q') \frac{(\eta_p^T \eta_q')^2}{|\eta_p| \, |\eta_q'|} \quad , \tag{2.61}
$$

where c and η denote the centers and normals of the faces of the meshes, $|\eta|$ is the mesh cell area, and k^W a Gaussian kernel with a fix width σ_W. By equation 2.60 every pair of normals in a neighborhood of size σ_W is considered and shape differences in the direction of normals are measured. In case of presence of holes and spikes in the mesh, the method is robust as it smoothens differences at a scale smaller than σ_W. When $S = S'$, the double sum scans every pair of normals p and q attached at different vertices of the mesh.

The only problem with this choice is that preparing the images to be compared with this current state of the software, needs changes in the input file at each time, while the procedure in using the Hausdorff criterion is only feeding the output file from the previous step to the MeshLab software.

The major benefit of the Deformetrica software can be considered in its capability to perform a deformable registration that is not applicable for our strategy and will not solve the problem of statistical approaches as well. It is so because even if the projection of a mean model completely matches with the patient's x-ray image by means of a nonrigid registration, still other views of the mean model are affected by all the bones in the dataset without considering their level of similarity with the patient's bone.

From a point cloud to the volumetric mesh two approaches can be employed. First one is considering the cortical and the trabecular thicknesses. Although the method seems reasonable but practically, a fixed thickness for the cortical is applied when it cannot be distinguished well (NAYLOR ET AL., 2013; SARKALKAN ET AL., 2014a; VÄÄNÄNEN ET AL., 2015).

TADDEI ET AL. (2006) measured the cortical thickness using CT scans; however, at the end, confirmed that the ambiguity in determining the thickness, acquiring mechanical properties from images, and the measurement of strains during experiments are sources of errors between results of the numerical simulations and the experiments.

Also considering the load points, TADDEI ET AL. (2006) has reported a procedure to exert the loads at exactly their same place in the experiments using markers on the bone and then registering them to find corresponding points on the simulated model. Another work that tried to address the issue is a numerical simulation by reporting the coordination of load points (HELLER ET AL., 2005); however, they did not mention the geometry of the bone model to enable performing the scaling later.

Regarding mesh convergence study two strategies can be applied: first the number of elements are investigated in which the amount of displacement and von Mises stress are changed within 1% at some of the marked elements while the number of elements is increasing. The second approach is averaging over four elements in specific sections of the bone. The pattern of the stress distribution is in agreement with former reports (see KANG ET AL., 1993; TADDEI ET AL., 2006); however, the absolute values are different which originates from differences in the geometry of the models and locations of the load points.

2.4 Conclusion

In this chapter, it was discussed that although employing SSMs are popular among researchers, their application needs to note some points. First, ethnic backgrounds, ages, and genders of patients in the dataset might be important and they need to be considered during building the SSM. Second, while projection of a mean model is modified to match well with the 2D images of a patient,

other views of the 3D mean model are still affected by the models in the dataset without considering their level of similarity to the patient's bone.

The presented method in this chapter was that: when the 3D model for a new patient was required who did not possess CT images, his x-ray image was divided in some parts. For instance, in a femur they were the head, the neck, the trochanter, and the shaft. Thereafter, the radiologist determined which part was the most important one and then the scaling ratio between the most important parts of the models in the dataset and the new patient's were calculated. Using the ratio, the 3D models in the dataset scaled afterward. The new models were then projected and their outlines were compared with the new patient's outline and one with the minimum Hausdorff distance was picked up as the 3D bone model of the new patient.

Using the ratio, the 3D models in the dataset scaled afterward. The new models were then projected, their outlines were compared with the new patient's outline and one with the minimum Hausdorff distance was picked up as the 3D bone model of the new patient.

Chapter 3

Error Analysis of the Steps of the Framework

Overview

- **Novelty**: Error analysis of the framework by performing new tests.

- **Method**: Previous works considered reproducibility of the interval steps of the framework only for the segmentation process. Arisen errors in other steps of the framework are measured in §3.2.1. Presenting a sequence in which accumulated errors of the steps of the framework are measured without considering the quality and quantity of the CT dataset is the topic of the second new test, §3.2.2. The next test is preformed similar to the former works which enables us to compare the reconstruction errors in this work with previous ones, §3.2.3. In the third new test, a relationship

between reconstruction errors and stress values are studied, §3.2.4.

3.1   Introduction

The final 3D bone model created by following the framework's steps in the previous chapter is not the same as the real bone model because of arisen errors in each step. To investigate these error values, accuracy tests in the former works were taken and they are classified in two types.

In the first, accuracy of segmentation was considered and they measured how much would be the difference between various segmented images. In the second type of the tests, it was examined how much would be the differences between two models built by the proposed method from 2D images of a patient and built from his CT scans, comparison between No.13 and No. 15, usually called validation test. As it can be seen, accuracy of other steps have not been addressed in the former works, e.g., how much the smoothing filter will affect the final model. In the first test, §3.2.1, this issue will be studied.

After performing the validation test, §3.2.3, a question arises whether application of the method on another dataset results in the same accuracy. The former works did not perform such an study which is the topic of the test two, §3.2.2. There a new sequence of steps are introduced which measures the error of the framework without considering the quality and quantity of the dataset.

Finally in the test four, §3.2.4, it is investigated how much the stress values will

change because of accumulated errors during the reconstruction. This is done by studying the difference of stress values on the areas with maximum reconstruction errors. The latter describes areas which are marked after comparing a reconstructed model with its gold model.

3.2   Methods and results

3.2.1   Test 1, Studying Accuracy of each Step of the Framework

This test is defined to measure reproducibility of the steps 2, 4, 6, and 8 and the arisen error by the smoothing operation. For the first four processes, the procedure of the test is that on a same input, the operation is performed three times and the results are compared by the Hausdorff criterion. Therefore, each of the operations, namely segmentation of a CT slice, No. 2, reconstruction of a surface model on a point cloud, No. 4, smoothing a surface model, No. 6, projecting a 3D model, No. 8, are performed three times and the obtained models at each step compared to each other.

The maximum occurred error in all the tests were less than 0.1 mm. But when the models resulted from smoothing, No. 5 and No. 7, were compared, the average error was 0.86 mm. Using the Hausdorff method the mean, the minimum and the maximum error values can be reported. Error here refers to the distance between similar points of the two compared models. In Fig. 3.1, the distances measured
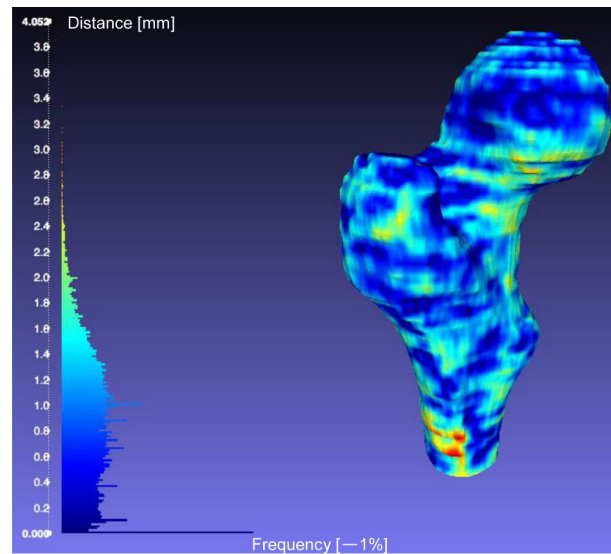
Figure 3.1: Distribution of the distances between corresponding points of two reconstructed models. The measurement criterion is the Hausdorff distance and a unit length of the frequency axis, (–), represents 1% of the total number of points.

by the Hausdorff method between two models are displayed. For instance, the

red areas represent those parts of the models which are in a distance of 4.2 mm.

3.2.2   Test 2, Verification Test of the Framework

In this test, the accuracy of the proposed method is studied regardless of the

quantity and quality of the dataset. The procedure is that the new patient, No.

10, is chosen from the database in No. 1 and then images at No. 13 and No. 15

of the framework are compared.

Thereby theoretically it is expected the framework results in a 3D model exactly

similar to the 3D reconstructed model of the patient's bone from the CT scans,

i.e. images No. 13 and No. 15 have to be exactly the same. However, practically

that does not happen and the measured error between the two images built by this strategy determines that kind of error.

Figure 3.2 shows that for 8 femurs of the training set, the average error between models No. 13 and No. 15 were less than $0.1\,\mathrm{mm}$, for one of them between $0.1\,\mathrm{mm}$ and $0.2\,\mathrm{mm}$, and so on. These values determine the error of the framework without considering the quality and quantity of the dataset which is called offset error. As the new patient's CT set was given in No. 1, it means both models in No. 13 and No. 15 were reconstructed from CT scans of the new patient. Therefore, the difference between models No. 13 and No. 15 was expected to be zero.
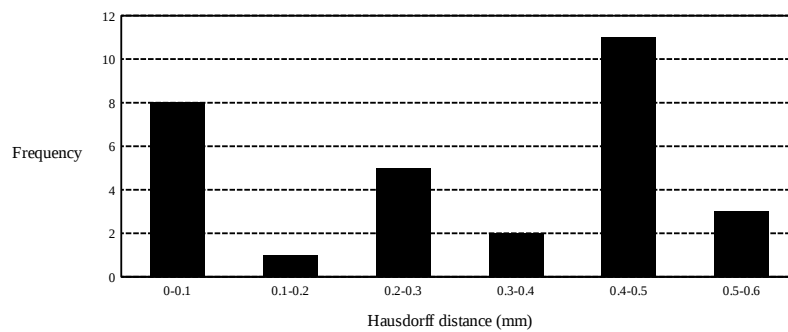
Figure 3.2: Frequency histogram of the reconstruction error measured for 30 models of the training set.

However, because of accumulated errors in the interval steps, No. 2, 4, 6, 8, and 11, the two models were not exactly the same and the average error between them for the femurs in the training dataset are displayed in Fig. 3.2. As for three models the error is a value between $0.5\,\mathrm{mm}$ and $0.6\,\mathrm{mm}$, it is concluded that the offset error of the framework using the implemented methods is $0.6\,\mathrm{mm}$. The

meaning of this number is that the framework cannot guarantee errors less than

0.6 mm.

3.2.3   Test 3, Validation Test of the Framework

Goal of this experiment is evaluation of the method similar to the approach re-

quired in clinical treatments. The procedure is that a new patient's 2D image is

given as input, No. 10, and the images No. 13 and No. 15 are then compared.
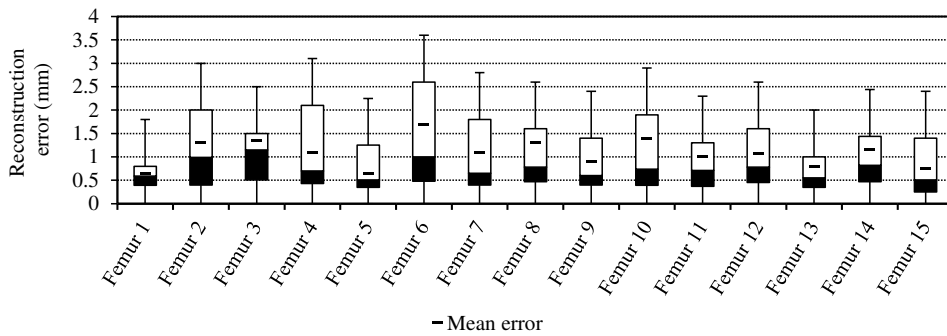
Figure 3.3: Reconstruction errors of 15 femurs in the validation group.

In Fig. 3.3 the reconstruction errors for femurs in the validation group are shown

in a box plot. The average errors shown by a solid line are less than 2 mm. As

the median values, top of the solid black rectangles, are nearer to the minimum

values, it is concluded that errors, the distances between corresponding points,

are mostly between the minimum and the median values.

3.2.4   Test 4, Investigating Changes in the Stress Distribution due to the Reconstruction Errors

This test is performed to investigate relationships between reconstruction errors and distribution of stresses on the femur models. In Fig. 3.4, the distribution of stress values on the models reconstructed from 2D and 3D images of one patient is shown. Assigning physical properties of bones, boundary conditions, and load forces were described in §2.2.7.

As can be seen, the amount of stress in the place of occurrence of maximum reconstruction error, red color areas in Fig. 3.1, on the femur reconstructed by the present method is $9.74\,\mathrm{MPa}$ and on the femur reconstructed from CT scans is $6.82\,\mathrm{MPa}$. If the difference between these two values is compared with the maximum stress value, the ratio is approximately $0.05 \approx [(9.74 - 6.82)/60]$ which means a reconstruction error of $4.2\,\mathrm{mm}$ causes change in the stresses at about 5% of the maximum stress value.

3.3   Discussion

In the first test, it was shown that smoothening a model could result in an average change of $0.86\,\mathrm{mm}$ on the surface bone model which was higher than reproducibility of the segmentation. It is true that using other smoothing filters can result in a value less than $0.86\,\mathrm{mm}$, but the intention is noting that when a new reconstruction method is introduced, this value is also required to be reported.
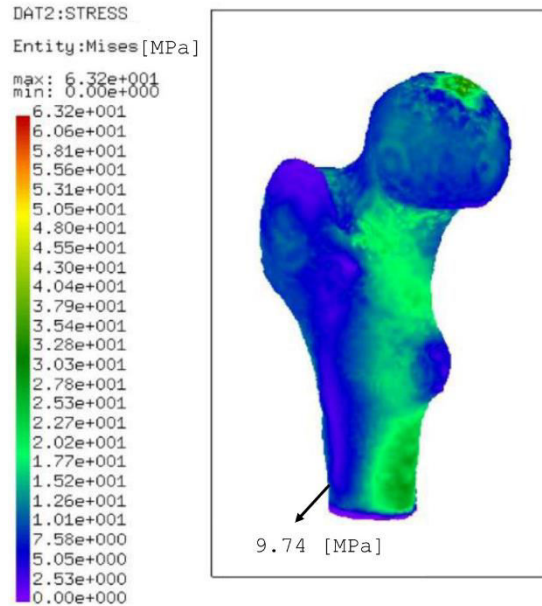
(a)
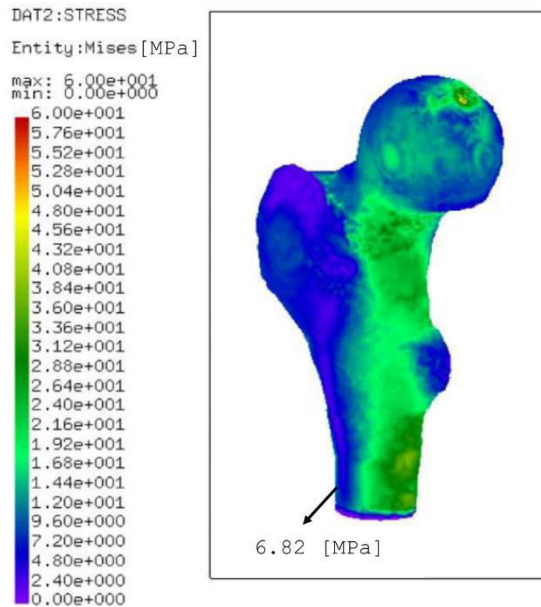
(b)

Figure 3.4: Von Mises stress field on a 3D model of a patient's femur reconstructed from his (a) 2D image, No. 13, and (b) CT scans, No. 15.

Former works did not mention reproducibility of other steps in their works while this value can be higher than the error of segmentation which they have tested (THEVENOT ET AL., 2013; VÄÄNÄNEN ET AL., 2015).

About the test two, §3.2.2, some of the former works instead of this test performed a leave-one-out test. The procedure was that CT scans of a patient from No. 1 was excluded and his x-ray image was given in No. 10. Then images No. 13 and No. 15 are compared. This procedure is exactly similar to what is performed in their next test, the validation test. The only difference is that they executed the leave-one-out test on the dataset at No. 1 and later did the validation test on another dataset, No. 10 (ZHENG ET AL., 2009; SARKALKAN ET AL., 2014a).

To discuss on the test three, §3.2.3, performing the validation test by the current regulation may not result in applicable information as its results depend on the similarity of bones in the training group at No. 1 and the test group at No. 10. To improve this analysis, it could be a suitable option to quantify the differences between the mean model and the new patient's bone model. That enables those who employed statistical approaches to find out how much difference between the mean models and new patients' bone models result in how much reconstruction errors.

Also about accuracy of this test, the criterion to measure the errors are different between works. SCHUMANN ET AL. (2010) used two methods and the difference between average errors did not change more than 0.5 mm. However, it is not clear

how much error values will change using a new measurement criterion. Therefore, a topic for a study might be quantifying this relationship. Another point to notice is that practically average errors are compared; however, the amount of maximum error and its position are also important to be determined.

3.4 Conclusion

In this chapter, accuracy tests in the former works were explained and new tests were introduced. In the first test, the arisen errors in each of the steps were investigated. The results showed that the smoothing's error could be larger than the segmentation's while in the literature this study was performed only for the segmentation. It might be argued if another smoothing method was applied, the error would become much smaller. This could be true but what the author suggested was that researchers in the field of 3D reconstruction should evaluate reproducibility of all the steps.

In the next test, the offset error of the method was investigated. That error determined the maximum level of reliability. The third test was the validation test and common among the former works. It was discussed that its results depended on the similarity of the images in the training group, No.1, and the test group, No. 10.

In the fourth test, changes in amount of the stress values due to the reconstruction errors were measured. The procedure for this test was that two reconstructed

bones of a patient, one built from CTs and one from 2D images, were undergone a same simulation, i.e., similar loading conditions and geometrical boundary conditions were applied to the both models. Then differences between stress values at the same areas were measured, e.g., where the maximum stress had happened in the reconstructed model from CTs. Using Hausdorff criterion, distances between these areas were also measured. Combination of these two measurements gave a new information that how much reconstruction error caused how much changes in the stresses.

Chapter 4

Acquiring mechanical properties from CT scans

Overview

- **Novelty**: Acquiring mechanical properties from CT scans without scanning a calibration phantom during the scanning.

- **Method**: To map material properties to the created models from x-ray images, it is required that the models in the CT dataset, contain the properties as well. For that purpose, i.e., assigning the material properties to the models in the CT dataset, in one of the possible approaches to perform this task in a patient-specific manner, calibration images had to be scanned during CT scanning the former patients. However, no calibration image was provided in the available CT dataset in this work. In §4.3.2 a method

is suggested to solve this problem.

4.1   Introduction

In chapters two and three, it was explained how to reconstruct a 3D model from x-ray images and the accuracy of the procedure was investigated. To perform FE simulation on the created models, it is required to assign physical properties of bones to the models. A feasible approach for this purpose is attributing mechanical properties to the 3D models in the CT dataset using their provided CT scans. Then a method similar to what was performed in chapter two is employed, i.e., finding the most similar bone parts and transferring their bone mineral density (BMD) values into the new model. However, this approach is faced with an obstacle which is lack of calibration images[1]. To solve this problem, a method is proposed in §4.3.2.

In the following first former works in the area of material mapping are reviewed and their methods are explained. Afterwards, the method to acquire physical properties from CT scans and the proposed method for calibrating CT machines are introduced.

---

[1]To obtain mechanical properties from CT scans, a calibration phantom has to be scanned. Then, a relationship between image intensities and bone mechanical properties is established using image processing techniques and experimental results. Thereafter, each voxel and, consequently, the bone model is attributed the properties (TADDEI ET AL., 2006).

4.2   Current Methods for the Material Mapping into the Meshed Bone Models

Assigning of material properties means that after generating a mesh, material properties have to be attributed to the elements. First approach is attributing constant properties to the whole cortical layer and doing the same for the trabecular areas. In this method, the cortical and the trabecular bone are meshed using respectively shell elements and brick elements. However, the shell-solid modeling's results are not in agreement with the experiments' (VARGHESE ET AL., 2011).

Thus, ZHANG ET AL. (2010) suggested that tetrahedral elements instead of shell elements should be used. Unstructured meshes provide the possibility that for each element, an average of properties of voxels encompassed by that element to be calculated and attributed to the element. However, it can cause underestimation or overestimation of the material properties, known as the partial volume effect (TADDEI ET AL., 2004).

In the second approach for the material mapping, a fixed Young's modulus for the cortical bone is considered, whereas the trabecular bone moduli is obtained by averaging the material properties over the finite elements inside the trabecular area (SHIM ET AL., 2008).

The third approach for translating the HU into mass density and Young's modulus is formulated in a thermodynamic framework. The reader can obtain a thor-

ough vision on former works in this area and learns its improvement performed in our research group by reviewing the following published dissertations and journal articles NACKENHORST (1997); EBBECKE (2006); LUTZ (2011); FIETZ (2013); SAPOTNICK & NACKENHORST (2014).

The fourth approach is finding a relationship between intensity of image voxels and the local mineral density of bone. In other words, stiffness of an enclosed piece of bone by a voxel is in relation with the Hounsfield unit (HU) value of the voxel. Therefore, through this approach, the non homogeneous nature of bone is considered as well (TANCK ET AL., 2009; CRAWFORD ET AL., 2003). Also, the partial volume effect and the need for detecting the cortical boundary layer during the segmentation are removed.

Among the four introduced approaches, only the last two can result in a patient-specific bone model. The third approach has been investigated formerly in our group. Therefore, the fourth method is studied in this work to enable us to compare the two approaches.

4.3   Method and Results

4.3.1   Calculating Physical Properties

In the following, the procedure to employ CT scans of a calibration phantom to acquire physical properties of bones is reviewed. The process has been implemented in the Bonemat software (TADDEI ET AL., 2006) and required steps are
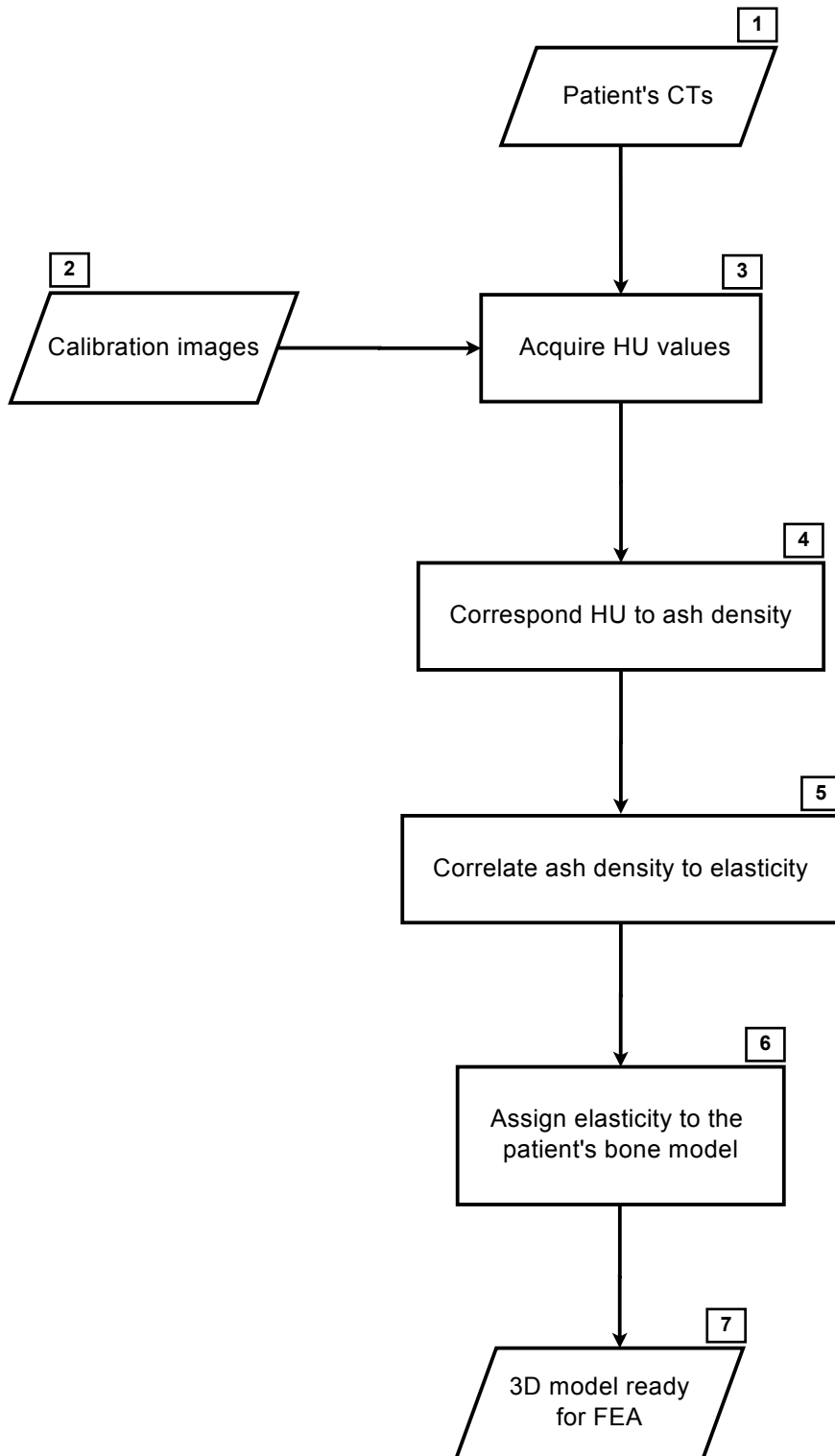
Figure 4.1: Schematic representation of the procedure to assign the elasticity to a bone model using a calibration phantom's scans.

shown in Fig. 4.1. For convenience in the description, the steps of the flowchart

are cited as No. X. The initial input data are given in No. 1 and No. 2 and then

in No. 3, the HU values are calculated. This step gives a relationship between

the HU values and the CT numbers. Thereafter in No. 4, the obtained HU values

are correlated to the ash density of the bone. The empirical relationships which

are utilized to connect these parameters are

$$\rho_{QCT} = 0.000791701(HU) - 0.00393573$$

$$\rho_{Ash} = 0.877\rho_{QCT} + 0.079$$

(4.1)

where ρ_{QCT} and ρ_{Ash} hold the unit of $\mathrm{g\,cm^{-3}}$ and respectively represent the hy-

drated tissue mass and the bone ash mass which are divided by the total specimen

volume. It is shown that a power law relationship relates the obtained density val-

ues to the Young's modulus (ZIOUPOS ET AL., 2008). One of the relationships

which matches well with experiments is

$$E = 14,664\,\rho_{Ash}^{1.49} \qquad,$$

(4.2)

where the Young's modulus, E, holds the unit of GPa (HELGASON ET AL.,

2008). Finally, the acquired elasticity for each voxel is attributed to the cor-

responding element in the meshed bone model, No. 6.

In Fig. 4.2 an output of the software is shown. The elasticity values changes

from 16.748 GPa to 10^{-6} GPa. The bone has maximum strength at outer rings of

the shaft and minimum strength at the middle of the femur. An important characteristic during evaluating osteoporosis for a patient is the strength of his femur neck. For that purpose two approaches in DEXA software are utilized.
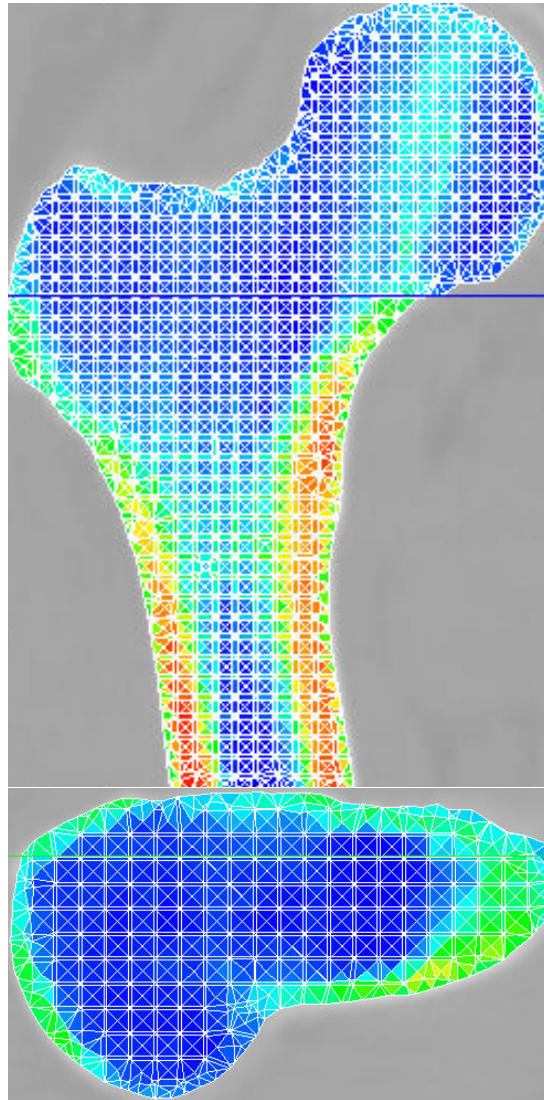
Figure 4.2: Distribution of the bone density (a) in a femur and (b) in a normal view to one of its sections. The red color represents the maximum elasticity value, equals to 16.748 GPa, and the dark blue color represents the minimum value, 10^{-6} GPa. Photo credit: reproduced from the data provided by the Institute of Istituto Ortopedico Rizzoli, Bologna, Italy.

First one is considering a section in the middle of the neck and calculating its BMD. Another approach is calculating the BMD at a section that is tangible with

the edge of the greater trochanter and normal to the neck axis. Using either of the approaches results in that the shown femur does not suffer from a decreased level of strength in the neck.

4.3.2   Calibration of CT Machines

Up to this state, it has been described how to assign density values to the bone models using calibration images which were scanned with them. However, when a dataset of CT scans are available but a calibration phantom has not been imaged with them, there is no approach in the literature describing how to do the calibration.

The method that is suggested in this section to solve this problem is based on assuming that effective parameters on the relationship between the CT numbers and the HU values in No. 3, are only the applied voltage and the current tube. This assumption is based on the results of a former study (GIAMBINI ET AL., 2015). It explored effects of various parameters on images of calibration phantoms and reported the applied voltage and the current tube as the key ones.

Our assumption concludes that if a phantom is scanned two times with a CT scanner, the obtained images are the same if the machine is run again with the same parameters as in the previous time. If it is proved, then the explained approach in Fig. 4.1 can be used again.

In such a case, when a set of CT scans is available without being accompanied

by any calibration image, one only needs to scan a phantom using the utilized CT machine while amounts of the parameters are set equal to the those applied for scanning the CTs. Thereafter, the obtained phantom's images are given as input at No. 2 and the procedure can continue similar to the described one in §4.3.1.
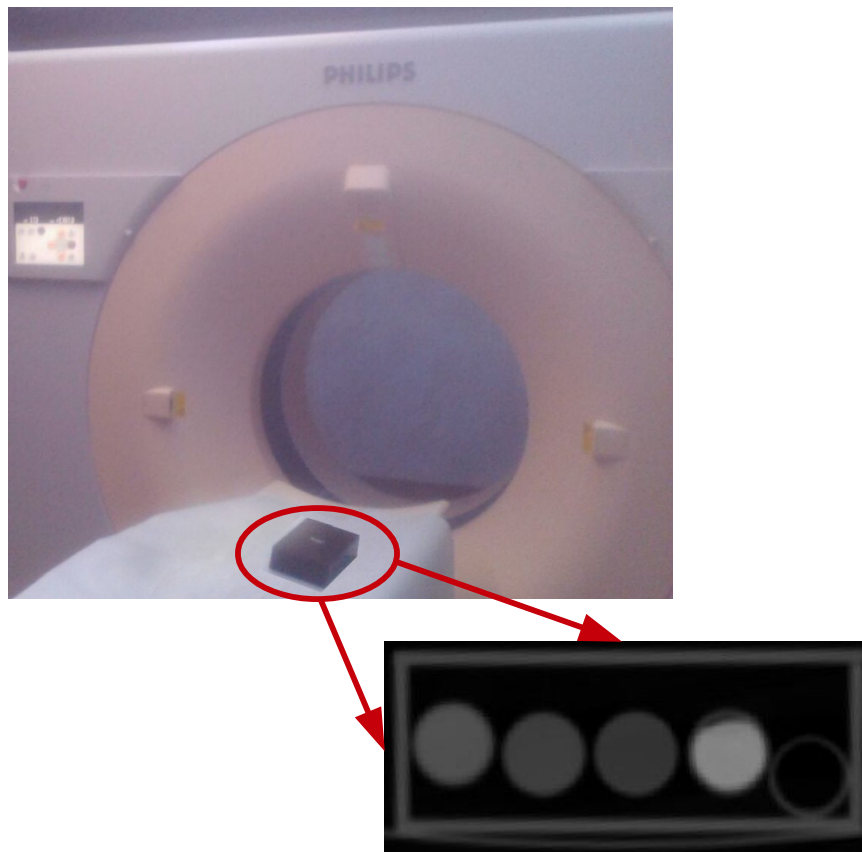
Figure 4.3: An experimental setup for studying the changes in the HUs when a scanner is run again without changes in the input parameters. The scanning acquisitions were obtained at a voltage of $120\,kV$, a current tube of $210\,mAs$, a collimation width of $80\,mm$, a slice thickness of $3\,mm$ and a spiral pitch factor of $0.914\,mm$. Photo credit: The experiment was performed by the author's own means; its result is hereby displayed for the first time.

The correctness of the assumption was investigated in an experiment as follows[2]:

a calibration phantom, calibrated against $CaCO_3$, were scanned three times using

---

[2]Perhaps it can be considered as a double-checking because GIAMBINI ET AL. (2015) has reported that the phantoms' images alter only because of changes in the voltage and the current tube.

an iCT 256 scanner (Philips, USA), Fig. 4.3. The voltage and the current were respectively set as $120\,\mathrm{kV}$ and $210\,\mathrm{mAs}$ in the exams.

The region of interest in the measurements were concentric circles with the rods[3] with a radius of 10 pixels. Increasing the radius to 16 pixels, covering 90% of the rod's area, did not change the numbers. Each measurement was performed three times and the average amount was assigned to the substance. The average values for the fat, the muscle and the bone changed less than 2% in the exams.

4.4   Discussion

Deriving the bone stiffness using HU values is based on assuming an isotropic behavior for the bone[4]; however, in reality, the bone consists of complex microstructures. The anisotropic behavior of the trabecular can be seen in its preferable growth direction (NEWITT ET AL., 2002).

To represent better this microstructure and, consequently, the macroscale behavior of the trabecular bone, one may apply a micro-FE model. However, this approach requires micro-CT images that is considered clinically incompatible. Furthermore, VERHULP ET AL. (2006) reports that the simplification of anisotropy by an isotropic behavior has little effects on the computed stress and strain distributions. However, this conclusion is valid only for healthy bones because the

---

[3]The calibration phantom composed of five rods, $\varnothing = 16\,\mathrm{mm}$ and $l = 13\,\mathrm{cm}$, Fig. 4.3. Each rod contained a reference material and the set was embedded in a plastic base material.

[4]During normalizing the HU values, a number of voxels are considered one unit and they are then assigned one intensity value. This action is based on assuming similar properties for all voxels in that unit which means ignoring the anisotropic behavior of the bone.

anisotropic behavior of the bone is an important parameter in the FE simulation of bones suffering from osteoporosis. Besides, in some bone areas, e.g., glenoid area, the physiological load is transferred due to the anisotropy ratio (CATTANEO ET AL., 2001; MANSAT ET AL., 1998).

It was explained that in one of the approaches for the material mapping, spatially varying material properties are applied, i.e., considering a fixed Young's modulus for the cortical bone, whereas the trabecular bone moduli is obtained by averaging the material properties over the elements (SHIM ET AL., 2008). Due to a large difference between Young's modulus of the cortical bone and the trabecular bone ($17\,\text{GPa}$ vs. $500\,\text{MPa}$), the cost of implementing such a meshing is higher than the strategy which considers a fixed value for the trabecular bone as well. However, it might be beneficial to perform a study in which the magnitude of ignoring the stiffness of the trabecular bone is investigated.

In the performed experiment, the 2% variation in the measured values, the CT numbers and, consequently, the HUs, can cause a change of $60\,\text{MPa}$ in the calculated elasticity, equation 4.2. This amount is about 10% of the elasticity of the trabecular bone, $500\,\text{MPa}$, and 0.35% of the elasticity of the cortical bone, $17\,\text{GPa}$. Therefore, one might conclude that the new method can be used for acquiring the properties from CT scans.

However, performing a study to investigate effects of the variations in the elasticity due to the application of the new method can be recommended. Also, conducting similar experiments with CT scanners from other producers might

be essential for application of the method on those machines.

The method removes the need to a calibration phantom during the screenings. If this feature is added to a current QCT software[5], normally taken scans can be fed into the software. For instance, currently in cases that the patient cannot meet the required body positioning for the imaging process, e.g., because of causing an extra pain, the software is simply out of function. Also in cases that the radiologist has not put the phantom in the correct field of view of the scanning, using the promoted software, there is no need to repeat the exam.

4.5   Conclusion

In this chapter, methods to assign physical properties to the bone models were reviewed. Thereafter, the procedure to use calibration images and acquiring the properties was described. In the following, an approach was presented for the purpose of the material mapping to the new patient's reconstructed bone model using a CT dataset. The method was that: during reconstructing the new patient's bone model, besides considering the geometry of the most similar bone in the dataset, its mechanical properties were also attributed to the new model.

Therefore, it was required that the obtained models from the CT dataset, contained material properties as well. To assign material properties to these

---

[5]Quantitative Computed Tomography (QCT), measures separately the cortical and the trabecular BMD in a volumetric state which makes it possible to use the results for reconstructing a patient-specific FE bone model (BESSHO ET AL., 2007; ADAMS, 2009; DRAGOMIR-DAESCU ET AL., 2011; WANG ET AL., 2012).

models, calibration images had to be scanned during CT scanning the former patients. However, no calibration image was provided in the available CT dataset.

To obtain the BMD from such CTs, an assumption was made that if a calibration phantom was scanned while the voltage and the current tube were set on the values which had been used during scanning the patient, the obtained images could be used for the calibration. The experiment showed that using the new method might cause a $60\,\mathrm{MPa}$ change in the computed elasticity.

Chapter 5

Conclusion

In chapter two of this work, it was discussed that although employing SSMs are popular among researchers, their application needs to note some points. First, ethnic backgrounds, ages, and genders of patients in the dataset might be important and they need to be considered during building the SSM. Second, while projection of a mean model is modified to match well with the 2D images of a patient, other views of the 3D mean model are still affected by the models in the dataset without considering their level of similarity to the patient's bone.

The presented method in this chapter was that: when the 3D model for a new patient was required who did not possess CT images, his x-ray image was divided in some parts. For instance, in a femur they were the head, the neck, the trochanter, and the shaft. Thereafter, the radiologist determined which part was the most important one and then the scaling ratio between the most important parts of the models in the dataset and the new patient's were calculated. Using

the ratio, the 3D models in the dataset scaled afterward. The new models were then projected and their outlines were compared with the new patient's outline and one with the minimum Hausdorff distance was picked up as the 3D bone model of the new patient.

In the next chapter, accuracy tests in the former works were explained and new tests were introduced. In the first test, the arisen errors in each of the steps were investigated. The results showed that the smoothing error could rise to higher amounts than the segmentation's while former works only studied the latter. It might be argued if another smoothing method was applied, the error would become much smaller. This could be true but what the author suggested was that researchers in the field of 3D reconstruction should evaluate reproducibility of all the steps.

In the next test, the offset error of the method was investigated. That error determined the maximum level of reliability. The third test was the validation test and common among the former works. It was discussed that its results depended on the similarity of the images in the training group, No.1, and the test group, No. 10.

In the fourth test, changes in amount of the stress values due to the reconstruction errors were measured. The procedure for this test was that two reconstructed bones of a patient, one built from CTs and one from 2D images, were undergone a same simulation, i.e., similar loading conditions and geometrical boundary conditions were applied to the both models. Then differences between stress

values at the same areas were measured, e.g., where the maximum stress had happened in the reconstructed model from CTs. Using Hausdorff criterion, distances between these areas were also measured. Combination of these two measurements gave a new information that how much reconstruction error caused how much changes in the stresses.

The accuracy of acquiring patient specific 3D models from limited number of 2D images could be influenced by the presence of the same model in the database. In other words, although a new method was suggested to overcome limitations of the former methods and also new tests were proposed to determine errors of the framework, the obtained values only determine the maximum level of confidence. Also, when a software based on the framework, creates a number of models with small values of error, there is no guarantee that for a new patient the reconstruction error does not reach to a larger amount because of, e.g., a genetic abnormality.

To overcome this problem, one plausible solution would be to employ such a software on a more specific target of patients. For instance the training set consists of patients with a special range of ages from one ethnicity with a specific kind of disease. Employing such a training set makes it more possible that when the software builds a 3D model for a new patient whose age, ethnicity and disease type is similar to the patients' in the training set, the reconstruction error would be in the expected range.

Nonetheless, the error could be so large because of a specific disease in the new

patient's bone. Therefore, about the future application of these methods to be applied in medical treatments, as x-ray images and CTs are mostly applied when the patient has a real problem and he is not a healthy person to perform an annual physical exam, it is highly expectable he possesses some unique features that methods based on databases cannot be applied for the treatment.

However, if the method is applied for reconstructing a 3D model from 2D images of a patient, e.g., during a surgery, while that patient was CT imaged before the operation, the method may be a wise selection. Through this approach, the patient receives less radiation dose, the cost of the treatment decreases and a high unexpected reconstruction error because of an unknown patient-specific disorder might not happen.

In the last chapter, methods to assign physical properties to the bone models were reviewed. Thereafter, the procedure to use calibration images and acquiring the properties was described. In the following, an approach was presented for the purpose of the material mapping to the new patient's reconstructed bone model using a CT dataset. The method was that: during reconstructing the new patient's bone model, besides considering the geometry of the most similar bone in the dataset, its mechanical properties were also attributed to the new model.

Therefore, it was required that the obtained models from the CT dataset, contained material properties as well. To assign material properties to these models, calibration images had to be scanned during CT scanning the former patients. However, no calibration image was provided in the available CT dataset.

To obtain the BMD from such CTs, an assumption was made that if a calibration phantom was scanned while the voltage and the current tube were set on the values which had been used during scanning the patient, the obtained images could be used for the calibration. The experiment showed that using the new method might cause a $60\,\text{MPa}$ change in the computed elasticity.

Appendix A

Implementation of the Framework in Software

In this section, the implementation of the framework introduced in chapter two is presented.

A.1   Step 2, Segmentation

For this purpose the itk-SNAP software [1] (V 3.4.0) is used, which is a free open-source and multi-platform software to segment structures of 3D medical images. In Fig. A.1 a common environment of the software is shown and the procedure resulting in a point cloud from DICOM images are listed below:

1- At the area marked 1 in Fig. A.1, click on the 'File' option and then 'Open' a DICOM image from the patient's CT images.

---

[1]http://www.itksnap.org
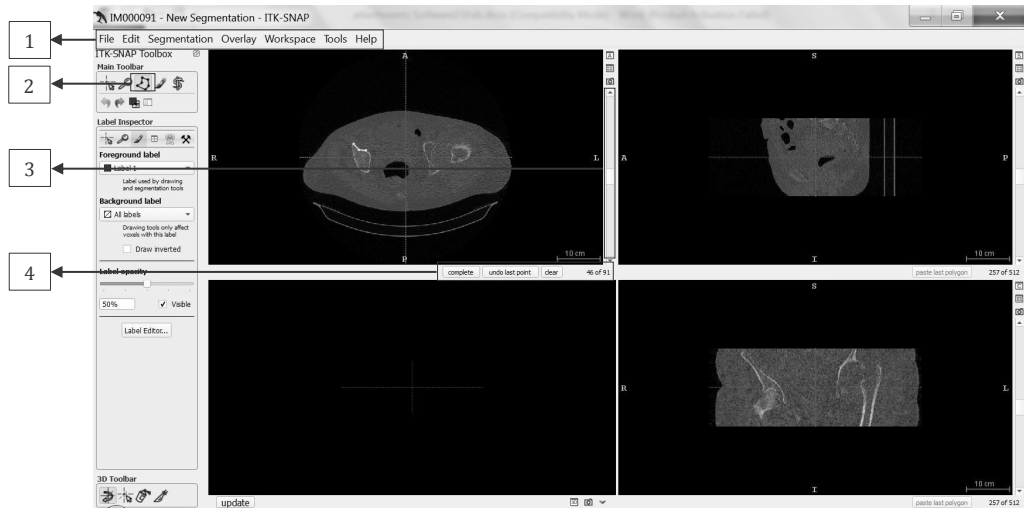
Figure A.1: The UI of the itk-SNAP software.

2- In the popped up window, set the file format as 'DICOM series', click on the area marked 2, and select the relevant pixels to be segmented.

3- Close the created polygon by clicking on 'Complete' in the area 4. Scroll among the slices using the side bar in 3 and repeat the segmentation.

4- Export the point cloud as '*.stl' by choosing 'Segmentation' in 1 and then the 'Export as surface mesh' option from the fallen down window.

A.2   Step 4 and 6, Surface Reconstruction and Smoothing

To reconstruct a surface on the resulted point cloud from the previous step and then smoothen the model, the Poisson method and the Taubin filtering imple-

mented in the MeshLab software [2] (V 1.3.3) are used. This software is free and can carry out various types of processing of 3D meshed models. Below is the list of steps required for the actions:

1- Click on the 'Filters' option at the main menu.

2- In the fallen down window, select the 'Remeshing, simplification and re-construction' option.

3- In the opened window, click on the 'Surface reconstruction: Poisson method'.

4- Click on the 'File' option in the main menu.

5- Select the 'Import mesh' from the fallen down window and choose the desired '*.stl' file.

6- Choose the option 'Unify duplicate vertices' in the popped out window.

7- Click on the 'Filters' in the main menu and choose the option 'Smoothing fairing and deformation'.

8- In the opened window, select the 'Taubin smooth' option.

9- Click on the 'File' option in the main menu, select 'Export mesh as' option in the fallen down menu and set the file type as: 'Object File Format (*.off)'.

---

[2]https://sourceforge.net/projects/meshlab

A.3   Step 8, Projection

The applied MATLAB[3] (Release 2014a, The MathWorks, Inc., Natick, Massachusetts, United States) code for this aim can be found in the supplementary materials and its algorithm is summarized as the below (letters in parentheses referred to the corresponding part in the code):

SET the initial parameters:

Detector panel size (A)

Distances between source to detector and to the object axis (B)

Gantry rotating direction (C)

Determining position of the object (D)

FOR all the required angles (E)

Project using the interp2 and the meshgrid commands in Matlab (F)

END

A.4   Step 11, Registration and Comparison the Outlines

The sequences to use the MeshLab software to measure the similarity between a bone in the dataset with the new patient's bone outline are as follows:

---

[3]https://www.mathworks.com/

I) The model in the dataset is scaled as in the following:

1- The 3D model in the dataset is projected. Its outline plus the new patient's bone outline are segmented using the itk-Snap software. The characteristic length from the 2D images, e.g., in a femur it can be the HD, ND, TW, or the SD, Fig. 2.6, is measured using the provided ruler in the Meshlab software. The scaling ratio is calculated by dividing these numbers.

2- Open the '.off' file of the 3D model. In the main menu, click on the 'Filters' tab and then choose the 'Normals, curvatures and orientation' option.

3- From the displayed options, choose the 'Transform: scale'. Write the scaling ratio in the 'Uniform scaling' box. Apply the changes and save them.

4- After projecting the new scaled 3D model, segment its outline and save it as a '.stl' file.

II) The two segmented outlines, one from the model in the dataset and one belongs to the new patient, are fed into the MeshLab and registered as in the following:

1- Click on the 'File' option in the main menu.

2- From the fallen down window, click on the 'Import' option and select the two '*.stl' meshes.

3- From the main menu click on the 'Edit' option.

4- From the fallen down window choose the 'Align' option.

5- Select the 'Iterative closest point registration (ICP)' option in the popped up window.

III) The two registered outlines are compared by the Hausdorff criterion as follows:

1- In the main menu, click on the 'Filters' option.

2- From the fallen down window, select the 'Sampling' option.

3- Among the appeared choices, choose the 'Hausdorff distance'.

4- From the main menu, click on the 'Edit' option.

5- From the choices in the popped out window, click on the 'Quality mapper' option.

6- From the main menu, click on the 'Render' option.

7- Choose the 'Show quality histogram' choice from the fallen down window to have the Hausdorff distance plus the minimum and the maximum distances.

A.5   3D Meshing of the Surface Mesh

Iso2mesh [4] (V 1.7.9), a free Matlab based mesh generation toolbox, which creates tetrahedral finite element meshes from surfaces is used for this purpose.

---

[4]http://iso2mesh.sourceforge.net

Below are a list of commands used to mesh the models:

1- Read the input file by running the relevant '*.m' file in the toolbox. The command is read as:

    [Node,Elem]=readoff('FileName.off');

2- Alter the surface to a volume at a given thickness. This can be done by the below commands:

    Img=s2v(Node,Elem);

    [Node1,Elem1,Face1]=v2m(Img,0.1,1,10);

3- To get a plot from the produced mesh, run the command:

    plotmesh(Node1,Face1)

4- To export the mesh in an appropriate format for the next software, it is written out by running the below command:

    mesh2abaqus(Node1,Elem1,'FileName');

A.6   FE Simulation of the Meshed Model

To perform the FE simulation, the CalculiX software [5] (V 2.10) is employed. It is an open set of Fortran codes that makes it possible to use this software to build FE models, calculate them by a linear and non-linear solver in static, dynamic,

---

[5]http://www.dhondt.de/

and thermal problems, and perform the post-processing. A compatible input file consists of the following parts (words in capital letters are predefined words in the software):

1- The input file is read by the command:

   *INCLUDE, INPUT=MeshFile.inp

   Note that to make the input file consistent with CalculiX, the line started with '*ELEMENT' in the 'MeshFile.inp' has to be replaced with:

   *ELEMENT, TYPE=C3D4, ELSET=Volume 3

2- Nodes that are later going to be constrained are read by

   *INCLUDE, INPUT=NodeFile.nam

3- To perform a linear elastic simulation, the Young's modulus and the Poisson's ratio are defined and set to the elements by:

   *MATERIAL, NAME=MAT

   *ELASTIC

    19E3,.3

   *SOLID SECTION, MATERIAL=MAT, ELSET=Volume3

4- The nodes that were read in the second line are fixed in three directions:

   *BOUNDARY

    Nfix,1

    Nfix,2

Nfix,3

5- Static loads are exerted. First the node number, then the load direction
(x, y, and z-directions are set as 1, 2, and 3 respectively), and finally its
amount are determined:

*STEP

*STATIC

*CLOAD

17897,1,4000

6- Required output parameters are determined. In this example displacements
U and stress values S are to be written by the commands:

*NODE FILE

U

*EL FILE

S

*END STEP

7- Save the input file as 'FileName.inp' and close it. Then open it by SciTE
editor, present in the downloaded folder, and start the simulation.

To perform post-processing on the acquired results, the procedure is as follows.

1- Run the '*.frd' file in the folder that the main files are present.
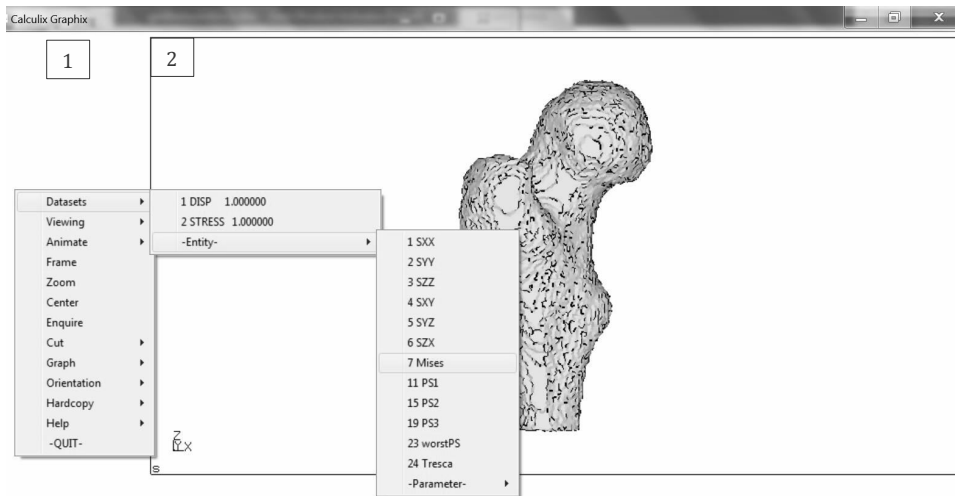
Figure A.2: The UI of the CalculiX software.

2- Click on the area marked 1 in the Fig. A.2 and select 'Dataset' among the

    appeared option. Then choose the desired parameters, e.g., stresses.

3- Click on 1 again and select 'Dataset'. Then choose the desired components

    to be displayed.

4- Turn off viewing the edge elements by

        view edges off

    During typing a command, the mouse pointer has to be kept on the area

    marked 2.

5- To increase the number of divisions that the parameter is shown, run the

    below command:

        steps <Desired number>

A.7 Increasing Quality of Meshes

To increase quality of the meshes, a free software, GmsH [6] (V 2.12.0), is used. The required steps to optimize the meshes and refine them are described in the following and the referred parts in the steps can be seen in the Fig. A.3.
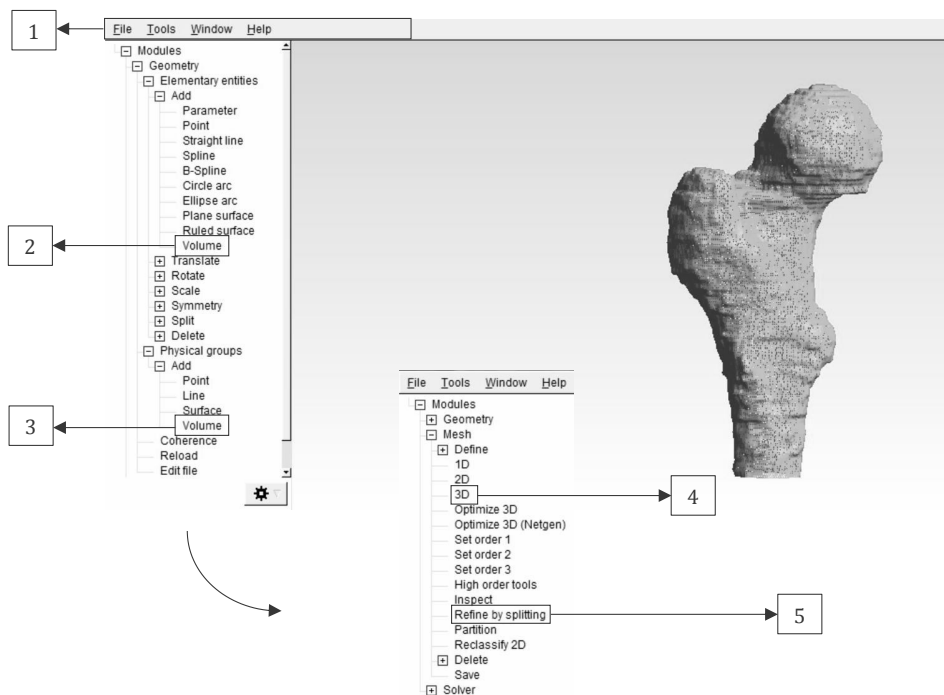
Figure A.3: The UI of the GmsH software.

1- In the area 1, click on the 'File' option and 'Open' the '*.stl' file of the model.

2- Click on the 'Volume' option at the area marked 2 and then select the opened '*.stl' model. Press the 'e' letter on the keyboard and 'Create new *.geo' file.

---

[6]http://gmsh.info

3- Select the bone model, press the 'e' letter on the keyboard, then click on the 'Volume' at the area 3, select the green ball inside the object and press the 'e' letter.

5- Select 'Tools' at the area marked 1, then 'Options' and select 'Mesh' from the popped up window.

6- In the tab 'Advanced', mark the two choices: 'Optimize quality of tetrahedra' and 'Optimize quality of tetrahedral with Netgen'.

7- Mesh the bone by selecting '3D' at the area marked 4. Use the area marked 5 to refine the mesh by determining an amount for splitting the elements.

Appendix B

Further Examples of the Femur and the Pelvis Reconstruction

In this section, 3D reconstruction of several models in the dataset are shown. The contribution of chapter two was introducing a new method for reconstruction of 3D models from 2D images and the results were shown and discussed there. Therefore, displaying other reconstructed models of femurs and pelvises may not have any impacts on the contribution. The goal of this section is providing a sign of proof that the suggested method is able to reconstruct other femur and pelvis models and it is not limited to the shown models in chapter two.

(a)

(b)

(c)

(d)

(e)
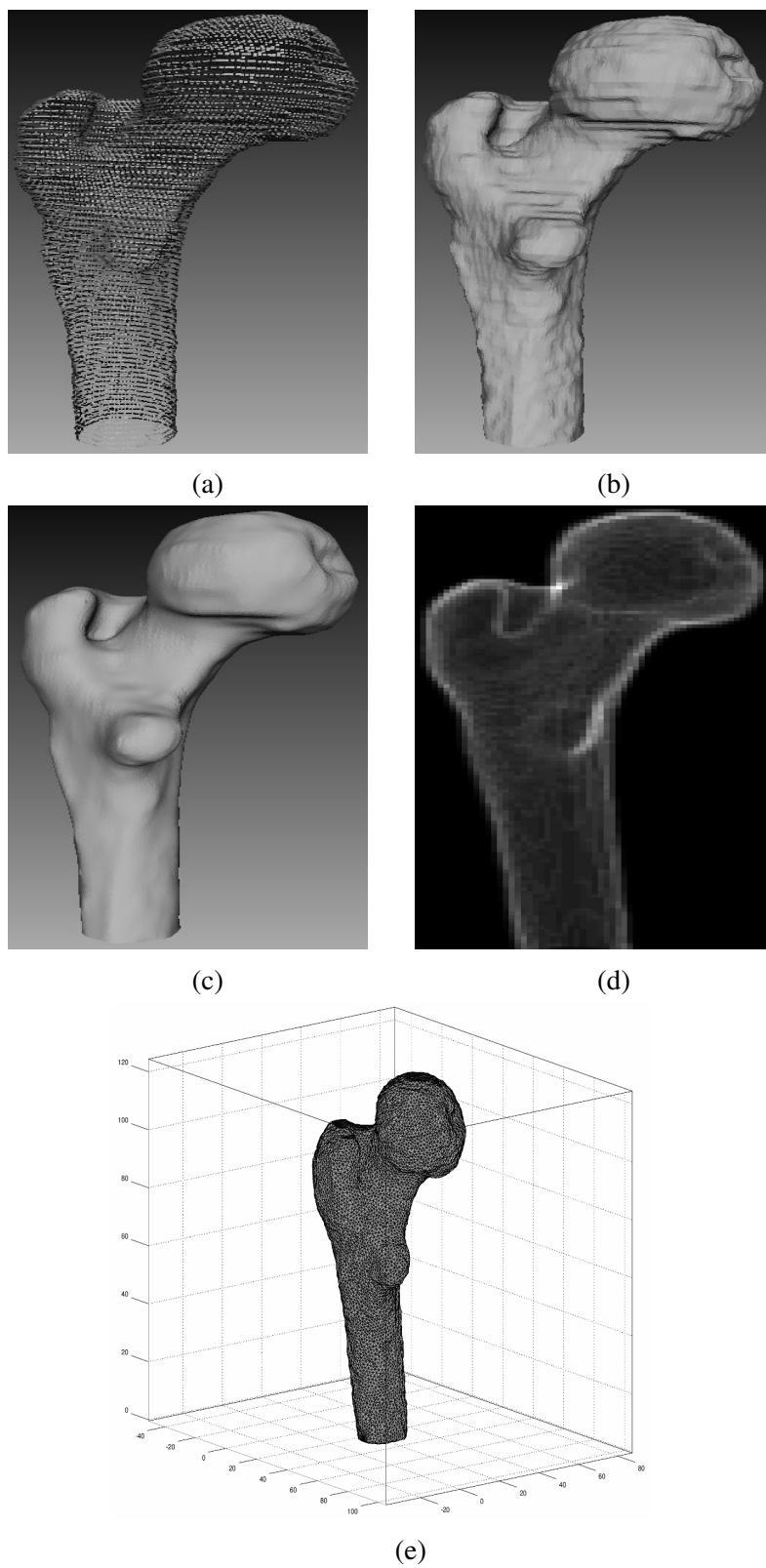
Figure B.1: Displaying the (a) point cloud, (b) reconstructed surface, (c) smoothened surface, (d) projected model, and (e) 3D mesh of a femur model in the dataset.

(a)   (b)

(c)   (d)

(e)
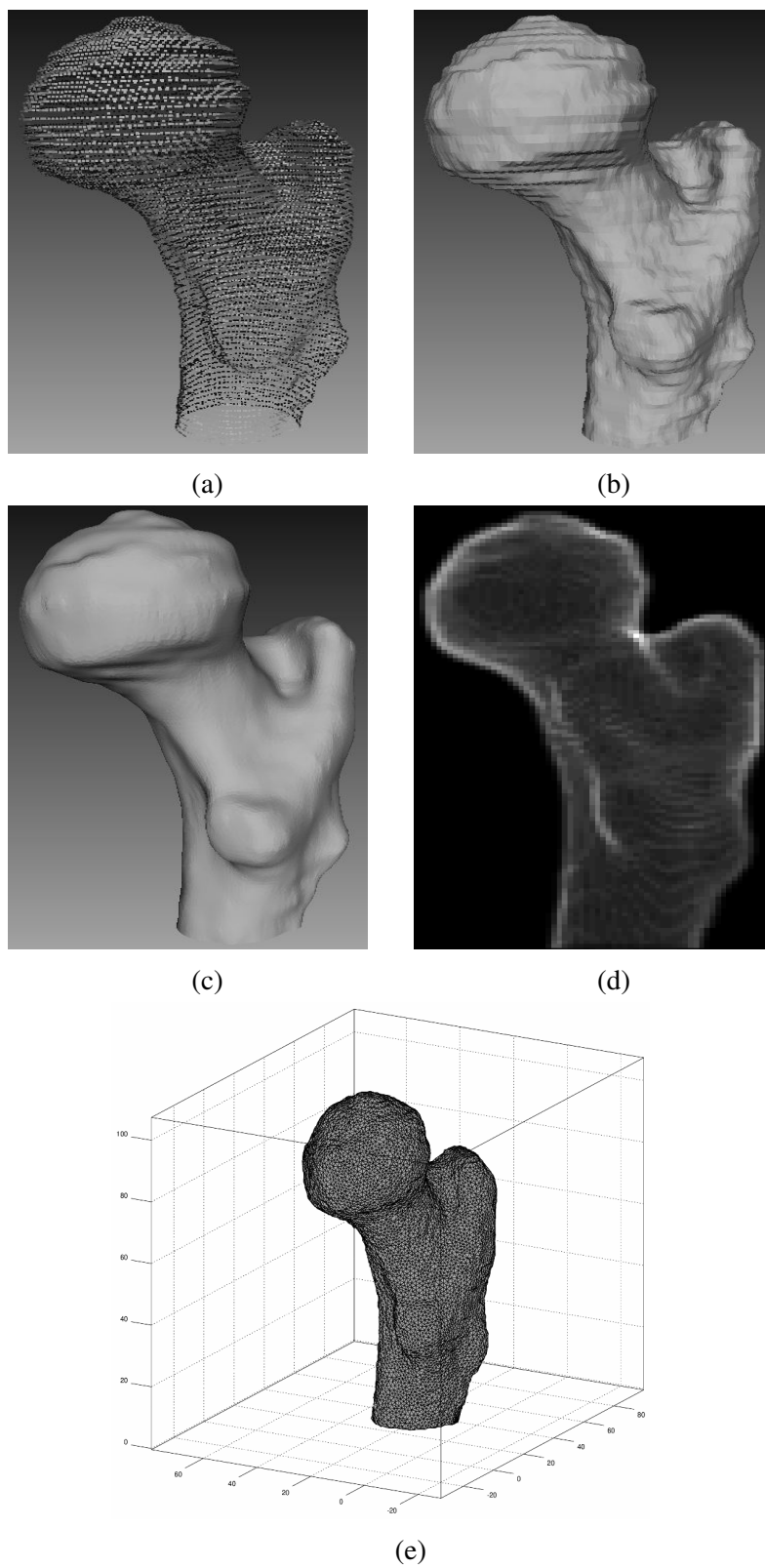
Figure B.2: Displaying the (a) point cloud, (b) reconstructed surface, (c) smoothened surface, (d) projected model, and (e) 3D mesh of a femur model in the dataset.
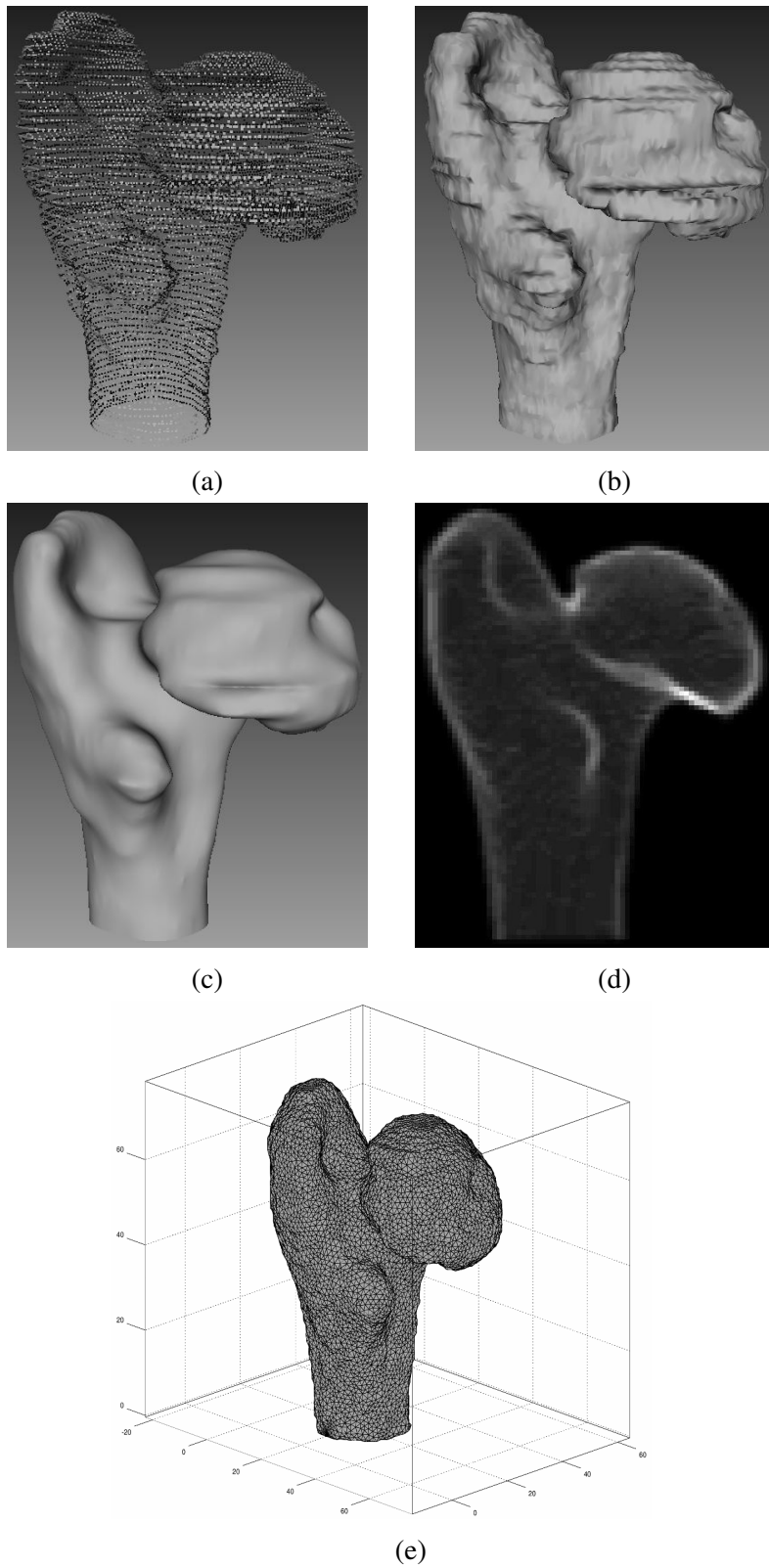
Figure B.3: Displaying the (a) point cloud, (b) reconstructed surface, (c) smoothened surface, (d) projected model, and (e) 3D mesh of a femur model in the dataset.

(a)

(b)

(c)

(d)

(e)
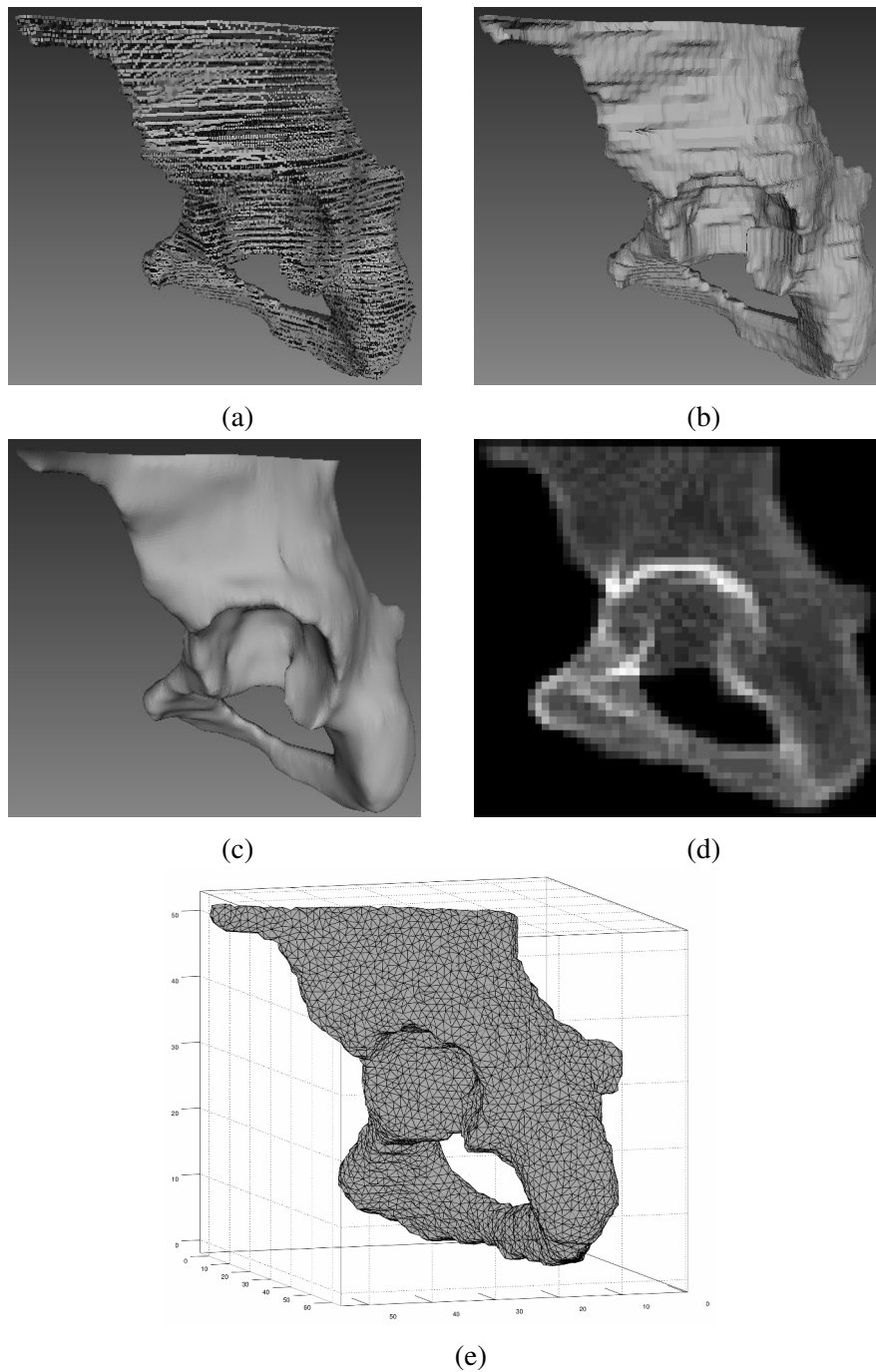
Figure B.4: Displaying the (a) point cloud, (b) reconstructed surface, (c) smoothened surface, (d) projected model, and (e) 3D mesh of a hemipelvis model in the dataset.
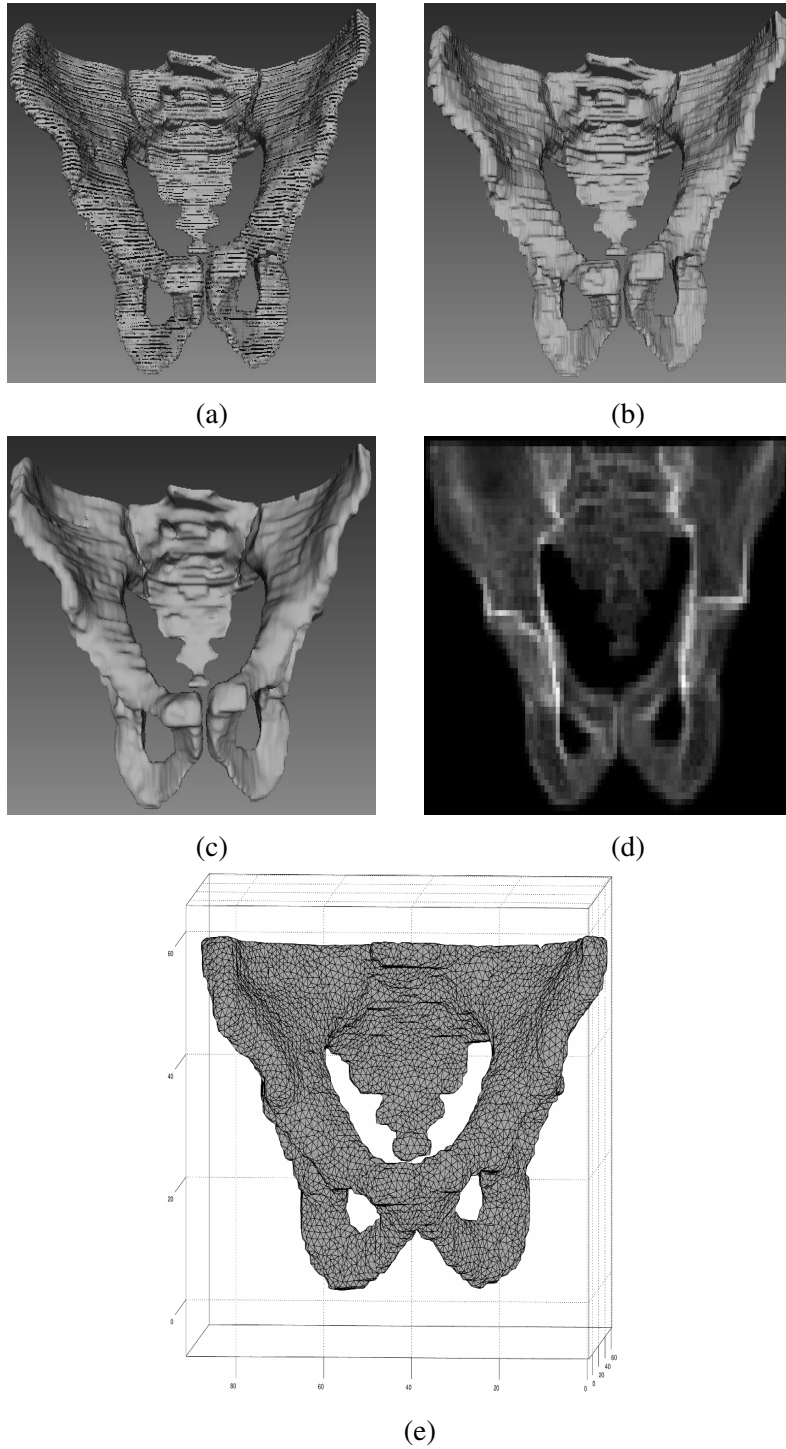
Figure B.5: Displaying the (a) point cloud, (b) reconstructed surface, (c) smoothened surface, (d) projected model, and (e) 3D mesh of a pelvis model in the dataset.

Bibliography

ADAMS J. Quantitative computed tomography. *European Journal of Radiology*, 71 (2009) (3): 415–424.

AMENTA N., BERN M. & KAMVYSSELIS M. A new voronoi-based surface reconstruction algorithm. In *SIGGRAPH '98, Proceedings of the 25th Annual Conference on Computer Graphics and Interactive Techniques*, pages 415–421. ACM, New York, NY, USA, 1998.

AMENTA N., CHOI S. & KOLLURI R.K. The power crust, unions of balls, and the medial axis transform. *Computational Geometry*, 19 (2001) (2): 127 – 153.

BAH M.T., SHI J., HELLER M.O., SUCHIER Y. ET AL. Inter-subject variability effects on the primary stability of a short cementless femoral stem. *Journal of biomechanics*, 48 (2015) (6): 1032–42.

BATHE K.J. *Finite-Elemente-Methoden*. Springer, 2002.

BESL P.J. & MCKAY H.D. A method for registration of 3D shapes. *IEEE Transactions on Pattern Analysis and Machine Intelligence*, 14 (1992) (2): 239–256.

BESSHO M., OHNISHI I., MATSUYAMA J., MATSUMOTO T. ET AL. Prediction of strength and strain of the proximal femur by a CT-based finite element method. *Journal of biomechanics*, 40 (2007) (8): 1745–1753.

BOISSONNAT J.D. Geometric structures for three-dimensional shape representation. *ACM Transactions on Graphics*, 3 (1984) (4): 266–286.

CATTANEO P.b.c., DALSTRA M.b. & FRICH L. A three-dimensional finite element model from computed tomography data: A semi-automated method. *Proceedings of the Institution of Mechanical Engineers, Part H: Journal of Engineering in Medicine*, 215 (2001) (2): 203–213.

CIGNONI P., ROCCHINI C. & SCOPIGNO R. Metro: Measuring error on simplified surfaces. *Computer Graphics Forum*, 17 (1998) (2): 167–174.

CRAWFORD R.c.f., CANN C.e. & KEAVENY T.b.c. Finite element models predict in vitro vertebral body compressive strength better than quantitative computed tomography. *Bone*, 33 (2003) (4): 744–750.

DEJACO A., KOMLEV V.S., JAROSZEWICZ J., SWIESZKOWSKI W. ET AL. Micro CT-based multiscale elasticity of double-porous (pre-cracked) hydroxyapatite granules for regenerative medicine. *Journal of Biomechanics*, 45 (2012) (6): 1068 – 1075.

DESERNO T.M. *Biomedical Image Processing*. Springer Science & Business Media, 2011.

DRAGOMIR-DAESCU D., OP DEN BUIJS J., MCELIGOT S., DAI Y. ET AL. Robust QCT/FEA models of proximal femur stiffness and fracture load during a sideways fall on the hip. *Annals of biomedical engineering*, 39 (2011) (2): 742–755.

DU S., ZHENG N., YING S., YOU Q. ET AL. An extension of the ICP algorithm considering scale factor. In *IEEE International Conference on Image Processing, ICIP 2007*, volume 5, pages 193–196.

DURRLEMAN S., PRASTAWA M., CHARON N., KORENBERG J.R. ET AL. Morphometry of anatomical shape complexes with dense deformations and sparse parameters. *NeuroImage*, 101 (2014): 35–49.

EBBECKE B. Theoretische und algorithmische konzepte zur beschreibung des beanspruchungsadaptiven knochenwachstums. *Institute für Baumechanik und Numerische Mechanik*, (2006).

EHLKE M., RAMM H., LAMECKER H., HEGE H.C. ET AL. Fast generation of virtual X-ray images for reconstruction of 3D anatomy. *IEEE transactions on visualization and computer graphics*, 19 (2013) (12): 2673–82.

FANG Q. & BOAS D. Tetrahedral mesh generation from volumetric binary and grayscale images. In *Biomedical Imaging: From Nano to Macro. ISBI '09. IEEE International Symposium on*, pages 1142–1145. 2009.

FIETZ K. Towards a finite element model for fluid flow in the human hip joint. *Institute für Baumechanik und Numerische Mechanik*, (2013).

GIAMBINI H., DRAGOMIR-DAESCU D., HUDDLESTON P.M., CAMP J.J. ET AL. The effect of quantitative computed tomography acquisition protocols on bone mineral density estimation. 137 (2015) (11): 114–120.

GONZALEZ R.C. & WOODS R.E. *Digital Image Processing*. Pearson Education, 2008.

GOOAYEN A., HERMANN E., WEBER G., GERNOTH T. ET AL. Model-based segmentation of pediatric and adult joints for orthopedic measurements in digital radiographs of the lower limbs. *Computer Science - Research and Development*, 26 (2011) (1-2): 107–116.

HALSTEAD M., KASS M. & DEROSE T. Efficient, fair interpolation using catmull-clark surfaces. In *Proceedings of the 20th Annual Conference on Computer Graphics and Interactive Techniques*, SIGGRAPH '93, pages 35–44. ACM, New York, NY, USA, 1993.

HAUSDORFF R.T. & WETS R.J.B. *Variational Analysis*. Springer Berlin Heidelberg, 1998.

HELGASON B., PERILLI E., SCHILEO E., TADDEI F. ET AL. Mathematical relationships between bone density and mechanical properties: A literature review. *Clinical Biomechanics*, 23 (2008) (2): 135–146.

HELLER M., BERGMANN G., KASSI J.P., CLAES L. ET AL. Determination of muscle loading at the hip joint for use in pre-clinical testing. *Journal of Biomechanics*, 38 (2005) (5): 1155 – 1163.

HELLMICH C., KOBER C. & ERDMANN B. Micromechanics-based conversion of CT data into anisotropic elasticity tensors, applied to FE simulations of a mandible. *Annals of Biomedical Engineering*, 36 (2008) (1): 108–122.

JOHANSSON T., MEIER P. & BLICKHAN R. A finite-element model for the mechanical analysis of skeletal muscles. *Journal of Theoretical Biology*, 206 (2000) (1): 131–149.

KAINMUELLER D. *Deformable Meshes for Medical Image Segmentation*. Springer, 2015.

KANG Y., PARK H., YOUM Y., LEE I. ET AL. Three dimensional shape reconstruction and finite element analysis of femur before and after the cementless type of total hip replacement. *Journal of Biomedical Engineering*, 15 (1993) (6): 497 – 504.

KARADE V. & RAVI B. 3D femur model reconstruction from biplane X-ray images: a novel method based on Laplacian surface deformation. *International journal of computer assisted radiology and surgery*, 10 (2015) (4): 473–85.

KAZHDAN M. & HOPPE H. Screened poisson surface reconstruction. *ACM Transactions on Graphics*, 32 (2013) (3): 1–13.

KOLLURI R., SHEWCHUK J.R. & O'BRIEN J.F. Spectral surface reconstruction from noisy point clouds. In *Proceedings of the 2004 Eurographics/ACM SIGGRAPH Symposium on Geometry Processing*, SGP '04, pages 11–21. ACM, New York, NY, USA, 2004.

LI C., XU C., GUI C. & FOX M. Distance regularized level set evolution and its application to image segmentation. *IEEE Transactions on Image Processing*, 19 (2010) (12): 3243–3254.

LUTZ A. Ein integrales Modellierungskonzept zur numerischen Simulation der Osseointegration und Langzeitsabilität von Endoprothesen. *Institute für Baumechanik und Numerische Mechanik*, (2011).

LUTZ A. & NACKENHORST U. Numerical investigations on the osseointegration of uncemented endoprostheses based on bio-active interface theory. *Computational Mechanics*, 50 (2012) (3): 367–381.

LUTZ A., NACKENHORST U., VON LEWINSKI G., WINDHAGEN H. ET AL. Numerical studies on alternative therapies for femoral head necrosis. *Biomechanics and Modeling in Mechanobiology*, 10 (2011) (5): 627–640.

MAHFOUZ M., FATAH E., BOWERS L. & SCUDERI G. Three-dimensional morphology of the knee reveals ethnic differences. *Clinical Orthopaedics and Related Research*, 470 (2012) (1): 172–185.

MANSAT P., BAREA C., HOBATHO M.C.B., DARMANA R. ET AL. Anatomic variation of the mechanical properties of the glenoid. *Journal of Shoulder and Elbow Surgery*, 7 (1998) (2): 109–115.

MARTINS J., PATO M. & PIRES E. A finite element model of skeletal muscles. *Virtual and Physical Prototyping*, 1 (2006) (3): 159–170.

MORETON H.P. & SÉQUIN C.H. Functional optimization for fair surface design. In *Proceedings of the 19th Annual Conference on Computer Graphics and Interactive Techniques*, SIGGRAPH '92, pages 167–176. ACM, New York, NY, USA, 1992.

NACKENHORST U. Numerical simulation of stress stimulated bone remodeling. *Technische Mechanik*, 17 (1997): 31–40.

NAYLOR K.E., MCCLOSKEY E.V., EASTELL R. & YANG L. Use of DXA-based finite element analysis of the proximal femur in a longitudinal study of hip fracture. *Journal of Bone and Mineral Research: The Official Journal of the American Society for Bone and Mineral Research*, 28 (2013) (5): 1014–1021.

NEWITT D., MAJUMDAR S., VAN RIETBERGEN B., VON INGERSLEBEN G. ET AL. In vivo assessment of architecture and micro-finite element analysis derived indices of mechanical properties of trabecular bone in the radius. *Osteoporosis International*, 13 (2002) (1): 6–17.

OSHER S. & SETHIAN J.A. Fronts propagating with curvature-dependent speed: Algorithms based on hamilton-jacobi formulations. *Journal of Computational Physics*, 79 (1988) (1): 12 – 49.

PETKOVIĆ T., HOMAN R. & LONČARIĆ S. Real-time 3D position reconstruction of guidewire for monoplane X-ray. *Computerized medical imaging and graphics : the official journal of the Computerized Medical Imaging Society*, 38 (2014) (3): 211–23.

ROBERTS M., COOTES T. & ADAMS J. Vertebral morphometry: Semiautomatic determination of detailed shape from dual-energy X-ray absorptiometry images using active appearance models. *Investigative Radiology*, 41 (2006) (12): 849–859.

ROBERTS M., OH T., PACHECO E., MOHANKUMAR R. ET AL. Semi-automatic determination of detailed vertebral shape from lumbar radiographs using active appearance models. *Osteoporosis International*, 23 (2012) (2): 655–664.

SAHA S. & ROYCHOWDHURY A. Application of the finite element method in orthopedic implant design. *Journal of Long-Term Effects of Medical Implants*, 19 (2009) (1): 55–82.

SAPOTNICK A. & NACKENHORST U. Mechanical stimulated biochemical fracture healing within a finite element framework. *Biomedical Engineering-Biomedizinische Technik*, 59 (2014): S1025–S1027.

SARKALKAN N., WAARSING J.H., BOS P.K., WEINANS H. ET AL. Statistical shape and appearance models for fast and automated estimation of proximal femur fracture load using 2D finite element models. *Journal of biomechanics*, 47 (2014a) (12): 3107–14.

SARKALKAN N., WEINANS H. & ZADPOOR A.A. Statistical shape and appearance models of bones. *Bone*, 60 (2014b): 129–40.

SCHUMANN S., LIU L., TANNAST M., BERGMANN M. ET AL. An integrated system for 3D hip joint reconstruction from 2D x-rays: A preliminary validation study. *Annals of Biomedical Engineering*, 41 (2013a) (10): 2077–2087.

SCHUMANN S., NOLTE L.P. & ZHENG G. Comparison of partial least squares regression and principal component regression for pelvic shape prediction. *Journal of Biomechanics*, 46 (2013b) (1): 197 – 199.

SCHUMANN S., TANNAST M., NOLTE L.P. & ZHENG G. Validation of statistical shape model based reconstruction of the proximal femur: A morphology study. *Medical Engineering and Physics*, 32 (2010) (6): 638 – 644.

SEIM H., KAINMUELLER D., HELLER M., LAMECKER H. ET AL. Automatic segmentation of the pelvic bones from CT data based on a statistical shape model. In *Proceedings of the First Eurographics Conference on Visual Computing for Biomedicine*, EG VCBM'08, pages 93–100. Eurographics Association, Aire-la-Ville, Switzerland, 2008.

SHEN C., O'BRIEN J.F. & SHEWCHUK J.R. Interpolating and approximating implicit surfaces from polygon soup. In *ACM SIGGRAPH 2004 Papers*, SIGGRAPH '04, pages 896–904. ACM, New York, NY, USA, 2004.

SHIM V., PITTO R., STREICHER R., HUNTER P. ET AL. Development and validation of patient-specific finite element models of the hemipelvis generated from a sparse CT data set. *Journal of Biomechanical Engineering*, 130 (2008) (5).

SPEIRS A.D., HELLER M.O., DUDA G.N. & TAYLOR W.R. Physiologically based boundary conditions in finite element modelling. *Journal of Biomechanics*, 40 (2007) (10): 2318–2323.

TADDEI F., CRISTOFOLINI L., MARTELLI S., GILL H. ET AL. Subject-specific finite element models of long bones: An in vitro evaluation of the overall accuracy. *Journal of Biomechanics*, 39 (2006) (13): 2457–2467.

TADDEI F., PANCANTI A. & VICECONTI M. An improved method for the automatic mapping of computed tomography numbers onto finite element models. *Medical Engineering and Physics*, 26 (2004) (1): 61–69.

TANCK E., VAN AKEN J., VAN DER LINDEN Y., SCHREUDER H. ET AL. Pathological fracture prediction in patients with metastatic lesions can be improved with quantitative computed tomography based computer models. *Bone*, 45 (2009) (4): 777–783.

TANG C.Y., ZHANG G. & TSUI C.P. A 3D skeletal muscle model coupled with active contraction of muscle fibres and hyperelastic behaviour. *Journal of Biomechanics*, 42 (2009) (7): 865–872.

TAUBIN G. A signal processing approach to fair surface design. In *Proceedings of the 22nd Annual Conference on Computer Graphics and Interactive Techniques*, SIGGRAPH '95, pages 351–358. ACM, New York, NY, USA, 1995.

THEVENOT J., KOIVUMÄKI J., KUHN V., ECKSTEIN F. ET AL. A novel methodology for generating 3D finite element models of the hip from 2D radiographs. *Journal of biomechanics*, (2013): 1–7.

TOMASZEWSKI P., VERDONSCHOT N., BULSTRA S., RIETMAN J. ET AL. Simulated bone remodeling around two types of osseointegrated implants for direct fixation of upper-leg prostheses. *Journal of the Mechanical Behavior of Biomedical Materials*, 15 (2012): 167–175.

VÄÄNÄNEN S.P., GRASSI L., FLIVIK G., JURVELIN J.S. ET AL. Generation of 3D shape, density, cortical thickness and finite element mesh of proximal femur from a DXA image. *Medical image analysis*, 24 (2015) (1): 125–34.

VARGHESE B., SHORT D., PENMETSA R., GOSWAMI T. ET AL. Computed-tomography-based finite-element models of long bones can accurately capture strain response to bending and torsion. *Journal of Biomechanics*, 44 (2011) (7): 1374–1379.

VERHULP E., VAN RIETBERGEN B. & HUISKES R. Comparison of micro-level and continuum-level voxel models of the proximal femur. *Journal of Biomechanics*, 39 (2006) (16): 2951–2957.

VUONG J. & HELLMICH C. Bone fibrillogenesis and mineralization: Quantitative analysis and implications for tissue elasticity. *Journal of Theoretical Biology*, 287 (2011): 115 – 130.

WANG X., SANYAL A., CAWTHON P.M., PALERMO L. ET AL. Prediction of new clinical vertebral fractures in elderly men using finite element analysis of CT scans. *Journal of bone and mineral research : the official journal of the American Society for Bone and Mineral Research*, 27 (2012) (4): 808–816.

WRIGGERS P. *Nonlinear Finite Element Methods*. Springer, Berlin, 2008.

XU D., CROCOMBE A. & XU W. Numerical evaluation of bone remodelling associated with trans-femoral osseointegration implant - A 68 month follow-up study. *Journal of Biomechanics*, 49 (2016) (3): 488–492.

YUSHKEVICH P.A., PIVEN J., HAZLETT H.C., SMITH R.G. ET AL. User-guided 3D active contour segmentation of anatomical structures: significantly improved efficiency and reliability. *NeuroImage*, 31 (2006) (3): 1116–28.

ZHANG Q.H., WANG J.Y., LUPTON C., HEATON-ADEGBILE P. ET AL. A subject-specific pelvic bone model and its application to cemented acetabular replacements. *Journal of Biomechanics*, 43 (2010) (14): 2722–2727.

ZHENG G. Statistical shape model-based reconstruction of a scaled, patient-specific surface model of the pelvis from a single standard AP x-ray radiograph. *Medical Physics*, 37 (2010) (4): 1424.

ZHENG G., GOLLMER S., SCHUMANN S., DONG X. ET AL. A 2D/3D correspondence building method for reconstruction of a patient-specific 3D bone surface model using point distribution models and calibrated x-ray images. *Medical Image Analysis*, 13 (2009) (6): 883 – 899.

ZIOUPOS P., COOK R. & HUTCHINSON J. Some basic relationships between density values in cancellous and cortical bone. *Journal of Biomechanics*, 41 (2008) (9): 1961–1968.

List of Figures

Curriculum vitae

Ehsan Jamshidi

Born 1987, Iranian

Professional Experience

04.2013 - 04.2016	Research assistant
	Institute of Mechanics and Computational Mechanics
	Leibniz Universität Hannover

Education

09.2010 - 09.2012	University of Tehran
	Mechanical Engineering
	Degree: M. Sc.
09.2005 - 09.2010	University of Tehran
	Mechanical Engineering
	Degree: B. Sc.
2001 - 2005	High school: Allame Helli, Tehran